

Effect of Loading Methods on Progressive Collapse Behavior of RC Beam-Slab Substructures under Corner Column Removal Scenario

Kai Qian[1,2*], Jian-Fei Cheng[1], Yun-Hao Weng[1], Feng Fu[3]

[1]College of Civil Engineering and Architecture, Guangxi University, Nanning, China, 530004.

[2]College of Civil Engineering and Architecture, Guilin University of Technology, Guilin, China, 541004.

[3]School of Mathematics, Computer Science and Engineering, City, University of London, U.K, EC1V 0HB.

Abstract: In this paper, high-fidelity finite element (FE) models were developed to investigate the behavior of reinforced concrete (RC) beam-slab substructures to resist progressive collapse under a corner column removal scenario. The numerical models were validated by test results. Then, the validated FE models were employed to investigate the structural behavior under different loading methods, including concentrated loading (CL) and uniformly distributed loading (UDL) methods. Moreover, multi-story frames were built to capture the load redistribution behavior of substructures at different floors under different loading methods. The results indicated that the loading methods affect overall structural responses, load transfer mechanisms, and failure modes. It was demonstrated that the Vierendeel action could not be ignored for multi-story frames to resist progressive collapse caused by the loss of a corner column scenario. More significant Vierendeel action was developed in the structure subjected to CL method than that subjected to UDL method. It was also found that the load transfer mechanisms developed in the top story and bottom story for a multi-story frame are pretty different from those in the middle stories. The bottom story has the most remarkable load resisting capacity.

Keywords: Progressive collapse; Loading method; Load transfer mechanism; Corner column removal.

* Corresponding author. E-mail address: qiankai@glut.edu.cn

1. Introduction

ASCE/SEI-10 (2010) [1] defines progressive collapse as the spread of an initial local failure from element to element, eventually resulting in the collapse of the entire structure or a large part of it disproportionately. Progressive collapse first attracted public attention after the partial collapse of Ronan Point apartment in London. The research topic became popular after the collapse of Alfred P. Murrah Federal Building in Oklahoma City and World Trade Center in New York. To date, several codes and design guidelines (ASCE/SEI-10 2010 [1]; General Services Administration (GSA) 2003 [2]; Department of Defense (DoD) 2009 [3]) had been issued for practical engineers to design buildings in mitigating progressive collapse. There are two main methods commonly suggested by design guidelines: direct and indirect design methods. Due to the uncertainty of extreme events, the alternate load path (ALP) method, one of the direct design methods, has been considered as a major technique as it is event-independent.

In the past decades, numerous experimental studies [4-18] and numerical simulations [19-25] have been conducted to investigate the progressive collapse behavior of reinforced concrete (RC) and precast concrete (PC) structures based on the ALP method. Remarkable efforts have been made towards deeper understanding of load transfer mechanisms, such as compressive arch action (CAA) [4-6], tensile catenary action (TCA) [7-9] developed in beams, and compressive membrane action (CMA) [11,12], tensile membrane action (TMA) in slabs [20,21]. Zhou et al. [4] conducted a series of static tests on a one-third scaled RC specimen and two PC specimens using dowel bars and corbel to investigate the load transfer mechanisms of these specimens under a middle column loss. Feng et al. [5] investigated the progressive collapse behavior of four beam-slab substructures subjected to a corner column loss. It was found that the development of TCA was limited due to weak horizontal constraints from the surrounding elements. Sasani [6] investigated the dynamic response of a 6-story RC frame subjected to simultaneous removal of a corner column and an adjacent exterior column. They concluded that the three-dimensional Vierendeel action plays a key role in load redistribution. It should be noted that the maximum vertical displacement was so low that no CAA and TCA were developed. Lu et al. [9] and Ren et al. [10] conducted several series of laboratory tests on RC specimens with or without slabs. In their tests, both the middle and edge column removal scenarios were investigated. It was found that the effects of beam height, slab thickness, and seismic reinforcing details dominate the progressive collapse resistance of RC frames.

It should be noted that the majority of existing tests relied on the concentrated loading (CL) method, which applied a concentrated load on the removed column. However, in reality, the load was uniformly distributed on the slab or beam. Thus, the uniformly distributed loading (UDL) method should be applied to represent real load patterns. However, for UDL method, the weights were increased slowly to simulate the increment of UDL, which should be very dangerous when reached the ultimate load capacity. In addition, the softening branch of the load-displacement curve could not be captured. To overcome this drawback, as an alternative method, the multi-points loading method (equivalent UDL), which was a displacement-controlled method, was widely adopted in previous investigations [15-19,21]. Qian et al. [15] carried out a series of RC beam-slab substructures under different column missing scenarios. The UDL method was equivalently applied on the slab by a specially designed loading frame. Pham et al. [17] also adopted the loading tree to equivalently apply UDL on progressive collapse performance of beam-slab substructures under the loss of an exterior column scenario. Moreover, flat slab or flat plate substructures were tested under the equivalent UDL method to investigate the effects of loading methods subjected to an interior column removal scenario [16,19].

The effects of loading methods on performance of RC substructures have been explored [18, 21]. The influence of loading methods on the behavior of buildings subjected to the loss of a corner column is still unclear due to insufficient investigations. Moreover, previous investigation was focused on single-story substructures [5,13], which has to ignore the Vierendeel action, one of the important load resisting mechanisms for RC frames subjected to the loss of a corner column scenario. Thus, in this study, high fidelity finite element (FE) models were developed to quantify the effects of different loading methods on the performance of RC frames to resist progressive collapse caused by the loss of a corner column scenario. Furthermore, multi-story frames were built to investigate the efficiency of Vierendeel action and quantify the mobilization of load transfer mechanisms among different stories with various loading methods.

2. Experimental program and numerical validation

2.1. Brief of the experimental program

Before conducting this numerical study, the FE model was validated by the experimental results of Feng et al. [5]. The experimental program [5] will be introduced briefly for readers easy to understand the validation and FE models. A seismically designed 6-story RC prototype building was designed following Chinese codes [26,27], with a height of 3900 mm in the first story and 3600 mm in upper stories. The span length in both directions was 5000 mm. The dead load (DL) and live load (LL) were 5.5 and 2.0 kPa, respectively. Four 1/2 scaled RC beam-slab substructures were tested subjected to the loss of a corner column scenario. However, only the results of Specimen US from Feng et al. [5] were used for validation in this study. The dimensions and reinforcement details of Specimen US are shown in Fig. 1. The overall dimension was 3200 mm × 3200 mm. The cross-section of the beam and column was 100 mm × 250 mm and 300 mm × 300 mm, respectively. The slab thickness was 70 mm. The transverse reinforcement was bent up 135° and was also installed in the beam-column joints in accordance with seismic RC detailing. The typical experimental setup and instrumentations are shown in Fig. 2. Three column supports were fixed to the RC blocks, which were fixed to the strong floor by bolts. To simulate the additional constraints from the surrounding slabs, a uniformly distributed load of 12.0 kN/m^2 was applied on the extending part of the slab. The load combination of (2DL+0.5LL) is selected, as suggested by GSA 2003 [2]. It should be noted that a one-way pin was installed between the hydraulic jack and the top of the corner column stub to allow the corner column stub to rotate and to ensure no extra bending will be introduced in the loading process. Thus, Vierendeel action of the frames can be neglected in this experimental program. A displacement-controlled CL manner was adopted.

The average cubic compressive strength of the concrete of Specimen US was 26.6 MPa, which corresponded to the cylinder compressive strength of 21.3 MPa. The measured reinforcement properties are tabulated in Table 1. For detail of test results, please refer to Feng et al. [5].

2.2. Numerical model setup

Commercial software LS-DYNA was adopted in this numerical study. Explicit solver was adopted to avoid divergence problems. The geometric model of Specimen US is shown in Fig. 3. Similar geometric dimensions, reinforcement details, and boundary conditions to the experimental test [5] were used in this numerical model.

2.2.1. Element types

As shown in Fig. 3, both concrete and steel plates were simulated by 8-node solid elements with a reducing integration scheme. There was one integration point in each solid element, which can considerably save computational time on the premise of accuracy when hourglass control is appropriately defined. To ensure the hourglass energy was less than 10% of the total internal energy, the hourglass coefficient was determined as 0.001. Flanagan-Belytschko stiffness form with exact volume integration was used. Moreover, reinforcements were modeled using 2-node Hughes-Liu beam elements with 2×2 Gauss quadrature integration. This beam formulation could effectively simulate the mechanical property of reinforcements, such as axial force, bi-axial bending, and transverse shear strain.

In this study, sensitivity analysis with three different mesh sizes of 25 mm, 20 mm, and 15 mm are conducted, as tabulated in Table 2. As shown in Fig. 4, mesh size of 20 mm is adequate, as further mesh refinement will not further enhance the accuracy significantly. As a result, the mesh size of concrete element is chosen as 20 mm × 20 mm × 17.5 mm for RC slabs and 20 mm × 20 mm × 20 mm for other components. The size of beam element is 20 mm.

2.2.2. Material model

Several constitutive models are available in the material library of LS-DYNA. In this study, continuous surface cap model (CSCM) is used for concrete as it could effectively simulate the mechanical property of concrete, including damage–based softening, modulus reduction, shear dilation, shear compaction, confinement effect, and strain rate effect [28]. The failure of CSCM model is controlled by the shear failure surface and hardening cap surface [29], as shown in Fig. 5. And the yield surface is formed based on three stress invariants J_1, J'_2, and J'_3. Previous studies [19-23] found that erosion criterion based on the maximum principal strain is a suitable way to simulate concrete crushing or spalling under both quasi-static and dynamic conditions. However, it could not simulate shear failure well when only the maximum principal strain was adopted for the definition of erosion criterion. Thus, Weng et al. [19] suggested that the maximum principal strain and shear strain criterions should be considered simultaneously by using keyword *Mat_Add_Erosion. Since the appropriate values are dependent on the mesh size, the value of maximum principal strain and shear strain is set to 0.08 and 0.3 based on multiple trials. Once the maximum principal strain or shear strain is reached, the solid element is deleted. Furthermore, the strain rate effect was ignored since only quasi-static behavior was discussed in this study.

LS-DYNA provides a simplified way to define CSCM (*Mat_CSCM_CONCRETE) for concrete properties, which only needs three input parameters (unconfined compressive strength $f_c^{'}$, maximum aggregate size A_g, and units). Then the remaining material properties are calculated automatically according to equations proposed by CEB-FIP concrete model code [30]. But the simplified CSCM is suited for $f_c^{'}$ between 28 MPa and 58 MPa. Since the unconfined compressive strength $f_c^{'}$ of Specimens US was 21.3 MPa, the original CSCM (*Mat_CSCM) is used, which requires a series of input parameters to define concrete material properties, as shown in Table 3.

However, the default concrete material properties would overestimate the initial stiffness and structural resistance, as shown in Fig. 6. Therefore, a few adjustments on the elasticity modulus and fracture energy of concrete were made to improve the numerical results. Previous studies [19-21,23] suggested that the tensile fracture energy G_{ft} could be reduced to 80% of the default one when it is over predicted. If shear or compressive-based damage is significant, the shear fracture energy G_{fs} should be set as $G_{fs} = 0.5G_{ft}$ and $G_{fc} = 50G_{ft}$. However, the default is $G_{fs} = 100G_{ft}$. In this study, since severe flexural and torsional failure occurred in the beam ends in Specimen US, both G_{ft} and G_{fs} were adjusted herein.

The detailed parameters of CSCM are listed in Table 3. The unconfined uniaxial stress-strain relationship of concrete after adjustments is shown in Fig. 7. The initial stiffness is lower than that of the default one, and the compressive stress reduces faster in the softening stage. As shown in Fig. 6, the adjusted material property could improve the numerical results significantly.

The symmetric bilinear elastic-plastic material model (*Mat_Plastic_Kinematic) is used for reinforcements, which assumes the tensile behavior is identical to that of compressive. The parameters of material properties, including elastic modulus, yield strength, tangential modulus, and ultimate strain, are determined based on the material tests. When the strain exceeds the ultimate elongation ratio, the corresponding reinforcement element is also deleted. The strain rate effect was ignored since only quasi-static behavior was discussed in this study. As suggested by previous works [19,23], a perfect bonding between concrete and reinforcement was assumed based on *Constrained_Lagrange_In_Solid.

2.2.3. Boundary conditions

In the numerical modeling, similar to the experimental program, the uniformly distributed load was applied on the extending area of the specimen. For simplicity, three concrete blocks were modeled using three rigid plates with zero translations and rotations, as indicated in Fig. 3. Furthermore, a rigid plate was generated at the top of the column stub to prevent stress concentration when concentrated loads were applied. Single surface (*Contact_Automatic_Single_Surface) was defined between the rigid plate and RC column. Besides, static and dynamic coefficients of friction were set as 1.0 at the contact surface to prevent any sliding of the rigid plate. Similar to experimental work, a one-way pin was generated between the loading plate and corner column by using constraint type *Constrained_Joint_Revolute.

2.3. Validation of the numerical model

Fig. 8 shows the comparison of load-displacement curves between the test results and FE model. At a large deformation, the TCA in beams and tensile membrane action in slabs is not efficiently mobilized due to the weak tie force from the surrounding structural members. Thus, the source of load resistance is mainly attributed to flexural action or beam action. As shown in Fig. 8, the load-displacement curve from FE model is quite similar to test results, including initial stiffness, yield load, ultimate load, and ultimate deformation capacity. The error of key results between the FE model and test one is less than 7 %, as listed in Table 4.

It is noted that the crack pattern of the RC beam-slab substructure cannot be directly demonstrated because concrete model CSCM is unable to track cracks. However, the cracks can be equivalently demonstrated by effective plastic strains. Generally, wider cracks expressed more significant effective plastic strains. The concrete damage was quantified through the damage index. Damage index of 0 and 1 represents no damage and complete failure, respectively. As shown in Figs. 9 and 10, FE model could effectively simulate concrete crushing or spalling of the beam and crack patterns of the slab.

As a result, the agreement of the load-displacement curves and the failure modes between the numerical and test results indicated the validity of the numerical model. Thus, the model was used to investigate the load transfer mechanisms of the RC frames with different loading methods and story numbers.

3. Effect of loading methods

Due to the limitation of cost and test conditions, only an experimental study under CL condition was conducted by Feng et al. [5]. However, UDL should be applied as gravity load and live load are uniformly distributed along the structure. Thus, it is necessary to study the difference between these two loading approaches. As a result, the validated FE model was utilized to evaluate the behavior of RC beam-slab substructures under both CL and UDL methods.

3.1. Details of UDL model

Previous studies [15-19,21] had proved the effectiveness of the 12-point loading tree to simulate the UDL scheme equivalently. Moreover, Weng et al. [19] modeled the load distribution rig with high fidelity, and the reliability of the numerical model was proved. Thus, in this study, the same modeling method was adopted to simulate the behavior of substructures under the UDL method. As shown in Fig. 11, the load distribution rig [19] consisted of a series of rigid beams and plates simulated by 8-node solid elements. The connection between the top and the secondary rigid beam was defined by keyword *Constrained_Joint_Revolute [19,21]. The connection between the secondary rigid beam and the triangle rigid plate was also modeled by keyword *Constrained_Joint_Revolute. The bottom steel plate was connected with the triangle steel plate by revolute joints to ensure the bottom plates could rotate. In addition, a contact function was used between the load distribution rig and RC frame by *Contact_Automatic_Single_Surface [19]. A one-way pin was also defined between the loading plate and the top rigid beam so that the top rigid beam was able to rotate around the one-way pin. In this study, each loading point coincided with the centroids of 12 sub-areas, as indicated in Fig. 12.

As shown in Fig. 13, a beam-slab substructure under the UDL method named US-UDL-1F was built based on the validated model of US-CL-1F. It should be noted that the dimensions, reinforcement details, and boundary conditions of US-UDL-1F are identical to those of US-CL-1F.

3.2. Structural resistance

Fig. 14 shows the comparison of the load-displacement curves from different loading schemes. As shown in the figure, the peak load of 43.7 kN and 250.6 kN was measured at US-CL-1F and US-UDL-1F, respectively. The initial stiffness, which is defined as the ratio of peak load to the corresponding displacement, of US-CL-1F and US-UDL-1F is 0.52 kN/mm and 5.2 kN/mm, respectively. Thus, the UDL method increases the peak load and initial stiffness by 473% and 897%, respectively. However, it should be noted that the load capacity from US-UDL-1F should be divided by four before comparing it with US-CL-1F based on a simple load distribution analysis. Thus, as shown in Fig. 14, the load-displacement curve of one-quarter of US-UDL-1F is generally more significant than that of US-CL-1F as the slab deformation of US-UDL-1F is more uniform. No major diagonal crack is formed, and more negative yield lines are observed at the top slab, as shown in Fig. 15.

3.3. Load redistribution of beam-slab substructures

To reveal the difference in load transfer mechanisms of the RC beam-slab substructures with different loading methods, the results of the internal forces of beams and columns were extracted. It should be noted that the beam sections are at a distance of 200 mm away from the beam-column interface to avoid element erosion and fail to provide the internal forces.

3.3.1. Development of axial force in beams

Fig. 16 shows the development of axial force at the cross-sections near the column stub. Due to symmetry, similar characteristics of axial force development are observed at cross-sections X-beam-1 and Y-beam-1. The axial force initially is compressive, indicating the mobilization of CAA. For CL and

UDL methods, when the displacement exceeds 370 mm and 296 mm, respectively, the axial force transfers into tension, reflecting the development of TCA.

The comparison between Fig. 16 (a) and (b) indicates that the UDL method significantly weakens the CAA of beams (e.g., the maximum axial compressive force reduces from 198.3 kN to 151.2 kN) but starts the TCA earlier and greater. For CL and UDL methods, the maximum axial tension force is 38.1 kN and 98.1 kN, respectively, which indicates that TCA is not efficiently mobilized due to fewer constraints from surrounding structural members.

3.3.2. Reactions of supporting columns

Figs. 17 (a) and (b) demonstrate the proportion of reaction force at different columns to the total reaction force under CL and UDL, respectively. For US-CL-1F, at the displacement of 50 mm, 44% and 44% of the load is distributed into columns B and D, respectively. Similarly, at this displacement stage, 42% and 42% of the load are distributed into columns B and D of US-UDL-1F. For US-CL-1F, after displacement of 82 mm, the proportion of columns B and D decreases with further increasing the displacement due to concrete crushing occurred at the beam AB and AD. Conversely, the proportion of column C keeps growing as column C remains almost intact during the test. However, for US-UDL-1F, after displacement of 20 mm, the proportion of columns B, C, and D nearly maintains constant because the deformation of the slab and beam is more uniform. In other words, column C suffers more significant damage when increasing the displacement.

3.4. Dynamic response

It is worth noting that progressive collapse is normally a dynamic event. Thus, it is necessary to evaluate the dynamic load capacity of the substructures under different loading methods. Based on previous studies [8,14,15,22], an energy-based model, which was proposed by Izzuddin et al. [31], was adopted in this dynamic evaluation. The dynamic resistance of the specimens could be determined by Eq. (1).

$$P_d(u_d) = \frac{1}{u_d}\int_0^{u_d} P_{NS}(u)\,du \quad (1)$$

where $P_d(u)$ and $P_{NS}(u)$ represent the dynamic load resisting function and nonlinear static load resisting function, respectively.

Fig. 18 illustrates the dynamic behavior of the beam-slab substructures. The dynamic peak loads of US-CL-1F and US-UDL-1F are 36.9 and 224.4 kN, respectively. Similar to the conclusions from nonlinear quasi-static results, the UDL method could increase the dynamic peak load by 508%. Even, the load resistance of US-UDL-1F is divided by four, the UDL method could increase the dynamic load capacity of CL-case by 52 %.

4. Analysis of multi-story frame structures

Progressive collapse is a global behavior for a multi-story building. However, only a single-story beam-slab substructure was tested in the test program [5]. Thus, it is imperative to understand whether the load transfer mechanisms in the single-story substructure are the same as those in a multi-story building. As shown in Fig. 19, US-CL-2F and US-UDL-2F were established, which represent a two-story frame substructure under CL and UDL methods, respectively. It should be noted that the load distribution tree, similar to US-UDL-1F, was generated in each story of US-UDL-2F.

4.1. The role of Vierendeel action

As concluded by Sasani [6], in moment frames, Vierendeel action is the major mechanism for the load redistribution of RC frames subjected to the loss of a corner column scenario. The Vierendeel action could resist the collapse of the buildings. For simplicity, due to the Vierendeel action, bending moment may develop in the beam end near the corner column to help the resistance of collapse.

Fig. 20 demonstrates the comparison of load resistance between single-story and two-story moment frames under both CL and UDL methods. The peak load of US-CL-1F, US-CL-2F, US-UDL-1F, and US-UDL-2F are 43.7 kN, 250.6 kN, 141.9 kN, and 525.2 kN, respectively. Thus, for CL method, the peak load of US-CL-2F is 324 % of that of US-CL-1F, which is much greater than the theoretical value of 200 %. The relatively large discrepancy could be attributed to Vierendeel action developed in US-CL-2F. For US-CL-1F, no Vierendeel action could be developed as the constraints from structural components in the upper story are ignored. However, the peak load of US-UDL-2F is 210 % of that of US-UDL-1F. Thus, comparing to CL method, the effects of Vierendeel action are quite limited. As mentioned above, the effects of Vierendeel action are expressed by developing positive moment at the beam end near the corner column. Thus, the mobilization of Vierendeel action may be reflected indirectly by the magnitude of shear force developed in the corner column. As shown in Fig. 21, much greater shear force develops in the corner column of US-CL-2F, comparing to US-UDL-2F.

4.2. Structural resistance from each story

Fig. 22 shows the comparison of the load resistance from different stories of a two-story frame with that from a single-story substructure. As shown in the figure, the load resistance of each story is different after the elastic stage. For CL method, compared with the single-story frame, the peak load of the first and second stories increases by 79 % and 58 %, respectively. However, under the UDL condition, the peak load of the first and second stories only increases by 7 % and 3 %, respectively. For both loading approaches, the bottom story achieves the greater load resisting capacity, which indicates that the Vierendeel action is more efficient in the bottom story, as the structural components in the second story could provide more significant constraints to the corner joint in the bottom story.

4.3. Load transfer mechanisms of multi-story RC frames

As aforementioned, the load transfer mechanisms in each story of the two-story frame are different. Thus, it is necessary to investigate load transfer mechanisms developing in each story of multi-story frames. Note that US-CL-3F, US-CL-4F, and US-CL-5F represent three-story, four-story, and five-story frame substructures under CL case, respectively. Similarly, US-UDL-3F and US-UDL-4F represent three-story and four-story frame substructures under the UDL case.

4.3.1. Structural resistance of multi-story frames

For US-CL-3F、US-CL-4F, and US-CL-5F, as shown in Fig. 23 (a), (b), and (c), the structural resistance developing in each story is different. The maximum load resistance is observed in the first story, which is the same as that found in US-CL-2F. By increasing the number of stories, it can be found that the initial stiffness, peak load, and residual load resistance of the middle story are pretty similar, which indicates that the development of load transfer mechanisms of the middle stories is almost identical. Moreover, the peak load of the middle stories is the least compared with the top and bottom ones. Like the CL case, for US-UDL-3F and US-UDL-4F, as shown in Fig. 24 (a) and (b), the bottom story also achieves the most significant initial stiffness and peak load. However, the difference of load resistance between the top story and the middle story is quite limited due to less Vierendeel action developed in UDL cases. In addition, due to the weak tie force from the surrounding elements, less TCA and TMA could be mobilized to resist progressive collapse under both CL and UDL methods. As shown in Fig. 23, comparing the load-displacement curve of the first story in models of US-CL-3F, US-CL-4F, and US-CL-5F shows that increasing the story number will not affect the load resistance and load transfer mechanisms of the first story. In other words, the constraints to the corner joint in the first story are similar whatever the story number is three, four, or five.

4.3.2. Axial force of beams in multi-story frames

Similar to what was discussed in section 3.3, the results of axial force in beams were also extracted to illustrate the load transfer mechanisms. For simplicity, only the cross-sections of beam AB were discussed herein. Note that the label of X-beam-1 to X-beam-5 represents the beams in the first to the fifth story, respectively.

As shown in Fig. 25, for CL case, the beams in each story are in compression before the displacement of 300 mm. After that, the axial force starts to decrease and changes into tension successively. Moreover, the beams in the first story begin to develop the CAA initially and achieve the maximum compressive force of 209.6 kN at the displacement of 112 mm. By contrast, beams in the top story achieve the maximum compressive force of 128.7 kN at the displacement of 214 mm, which indicates lower CAA developed in top story. Moreover, the compressive force is the least in the middle story compared with the top and first stories. Similarly, for UDL case, as shown in Fig. 26, the largest compressive force of 106.3 kN is measured in the first story. Moreover, the compressive force in the beams in the top story is slightly larger than that in the middle story.

For both loading methods, it is observed that the axial force of beams in the middle stories is similar, which agrees well with the results of load resistance.

5. Conclusions

Based on the numerical and parametric study conducted in this study, the following conclusions are drawn:

1. Compared with experimental results, it is found that the high-fidelity numerical models can simulate the global behavior of the RC beam-slab substructure subjected to a corner column loss scenario well. However, the shear fracture energy should be adjusted to well simulate the stiffness of the concrete in CSCM.

2. For single-story models under either UDL or CL methods: US-UDL-1F and US-CL-1F, the peak load of US-UDL-1F is 537 % of that US-CL-1F, which is greater than the theoretical value of 400%. Thus, it indicates that the simplified CL method may underestimate the load resistance of the beam-slab substructures subjected to the loss of a corner column scenario. It could be explained as UDL method may achieve more uniform deformation of the beam and slab, and thus, more materials could be fully mobilized.

3. For multi-story models, it was found that Vierendeel action could not be ignored to resist progressive collapse of RC frames caused by the loss of a corner column scenario. Comparing to multi-story frames subjected to UDL method, the Vierendeel action has more significant effects on the frames under CL method. As the building was subjected to UDL load, in reality, the commonly used CL method may overestimate the contribution of Vierendeel action. Moreover, the Vierendeel action is more efficient in lower stories than that in the upper stories. Therefore, in practical design, it was suggested to apply UDL load and generating multi-story frames to obtain more accurate results.

4. The numerical results indicated that the load transfer mechanisms developed in different stories are

not identical for a multi-story frame subjected to the loss of a corner column scenario. Moreover, it was found that increasing the story number will not affect the load resistance and load transfer mechanism of the first story.

References

[1] ASCE/SEI 7, Recommendations for Designing Collapse-Resistant Structures, Structural Engineering Institute-American Society of Civil Engineers, Reston, VA, 2010.

[2] GSA, Progressive Collapse Analysis and Design Guidelines for New Federal Office Buildings and Major Modernization Projects, U.S. General Service Administration, Washington, DC, 2003.

[3] Department of Defense (DoD), Design of Building to Resist Progressive Collapse. Unified Facility Criteria, UFC 4-023-03, US Department of Defense, Washington (DC), 2009.

[4] Y. Zhou, T.P. Chen, Y.L. Pei, H.J. Hwang, X. Hu, W.J. Yi, L. Deng, Static load test on progressive collapse resistance of fully assembled precast concrete frame structure, Eng. Struct. 200 (2019) 109719.

[5] P. Feng, H.L. Qiang, X. Ou, W.H Qin, J.X Yang, Progressive collapse resistance of GFRP-strengthened RC beam–slab subassemblages in a corner column–removal scenario, J. Compos. Constr. 23 (2018) 04018076.

[6] M. Sasani, Response of a reinforced concrete infilled-frame structure to removal of two adjacent columns, Eng. Struct. 30(9) (2008) 2478-2491.

[7] K. Qian, S.L. Liang, F. Fu, Y Li, Progressive collapse resistance of emulative precast concrete frames with various reinforcing details, J. Struct. Eng. 147(8) (2021) 04021107.

[8] X.F. Deng, S.L. Liang, F. Fu, K. Qian, Effects of high-strength concrete on progressive collapse resistance of reinforced concrete frame, J. Struct. Eng. 146(6) (2020) 04020078.

[9] X.Z. Lu, K.Q Lin, Y. Li, H. Guan, P.Q. Ren, Y.L. Zhou, Experimental investigation of RC beam-

slab substructures against progressive collapse subject to an edge-column-removal scenario, Eng. Struct. 149 (2017) 91-103.

[10] P.Q. Ren, Y. Li, X.Z. Lu, H. Guan, Y.L. Zhou, Experimental investigation of progressive collapse resistance of one-way reinforced concrete beam-slab substructures under a middle-column-removal scenario, Eng. Struct. 118 (2016) 28-40.

[11] N.S. Lim, K.H. Tan, C.K. Lee, Experimental studies of 3D RC substructures under exterior and corner column removal scenarios, Eng. Struct. 150 (2017) 409–427.

[12] A.T. Pham, N.S. Lim, K.H. Tan, Investigations of tensile membrane action in beam-slab systems under progressive collapse subject to different loading configurations and boundary conditions, Eng. Struct. 150 (2017) 520–536.

[13] K. Qian, B. Li, Slab effects on response of reinforced concrete substructures after loss of corner column, ACI Struct. J. 109 (6) (2012) 845–855.

[14] K. Qian, B. Li, J.X. Ma, Load-carrying mechanism to resist progressive collapse of RC buildings, J. Struct. Eng. 141(2) (2015) 04014107.

[15] K. Qian, B. Li, Z. Zhang, Influence of multicolumn removal on the behavior of RC floors, J. Struct. Eng. 142 (5) (2016), 04016006.

[16] K. Qian, B. Li, Load-resisting mechanism to mitigate progressive collapse of flat slab structures, Mag. Concr. Res. 67 (7) (2015) 349–363.

[17] P.X. Pham, K.H. Tan, Experimental response of beam-slab substructures subject to penultimate-external column removal, J. Struct. Eng. 141(7) (2015) 04014107.

[18] X.D. Pham, K.H. Tan, Experimental study of beam–slab substructures subjected to a penultimate-internal column loss, Eng. Struct. 55 (2013) 2–15.

[19] Y.H. Weng, K. Qian, F. Fu, Q. Fang, Numerical investigation on load redistribution capacity of flat slab substructures to resist progressive collapse, J. Build. Eng. 29 (2020) 101109.

[20] K. Qian, Y.H. Weng, F. Fu, X.F. Deng, Numerical evaluation of the reliability of using single-story substructures to study progressive collapse behaviour of multi-story RC frames, J. Build. Eng. 33 (2021) 101636.

[21] J. Yu, L. Luo, Y. Li, Numerical study of progressive collapse resistance of RC beam-slab substructures under perimeter column removal scenarios, Eng. Struct. 159 (2018) 14-27.

[22] A.T. Pham, K.H. Tan, J. Yu, Numerical investigations on static and dynamic responses of reinforced concrete sub-assemblages under progressive collapse, Eng. Struct. 149 (2017) 2-20.

[23] J. Yu, Y.P. Gan, J. Wu, H. Wu, Effect of concrete masonry infill walls on progressive collapse performance of reinforced concrete infilled frames, Eng. Struct. 191 (2019) 179-193.

[24] Y. Li, X.Z. Lu, H. Guan, L.P. Ye, An improved tie force method for progressive collapse resistance design of reinforced concrete frame structures. Eng. Struct. 33(10) (2011) 2931–2942.

[25] D.C. Feng, S.C. Xie, J. Xu, K. Qian, Robustness quantification of reinforced concrete structures subjected to progressive collapse via the probability density evolution method, Eng. Struct. 202 (2020) 109877.

[26] Ministry of Housing and Urban-Rural Development of the People's Republic of China (MOHURD). Code for design of concrete structures. GB50010-2010. Beijing, China; 2010.

[27] Ministry of Housing and Urban-Rural Development of the People's Republic of China (MOHURD). Code for seismic design of buildings, GB50011-2010. Beijing, China; 2010.

[28] Y. Wu, J.E. Crawford, J.M. Magallanes, Performance of LS-DYNA concrete constitutive models, 12th Int. LS-DYNA Users Conf, Livermore Software Technology Corporation, Livermore, CA, 2012.

[29] J. Hallquist, LS-DYNA Keyword User's Manual, Version 971, Livermore Software Technology Corp., Livermore, CA, 2007.

[30] CEB. CEB-FIP model code 1990. Thomas Telford; 1991.

[31] B.A Izzuddin, A.G Vlassis, A.Y Elghazouli, D.A Nethercot, Progressive collapse of multi-storey buildings due to sudden column loss — Part I: Simplified assessment framework, Eng. Struct. 30(5) (2008) 1309–18.

Captions of tables

Table 1-Reinforcement properties

Table 2-Study on different mesh sizes

Table 3-Model parameters of CSCM for FE models (Unit: N, mm and ms)

Table 4-Comparison of key results between test and FE model

Captions of figures

Fig. 1–Dimensions of specimen US (units: mm) [5]

Fig. 2–Test setup and instrumentation location in the referenced experiment [5]

Fig. 3–Numerical model of US-CL-1F

Fig. 4–Comparison of different mesh sizes

Fig. 5–General shape of concrete model yield surface

Fig. 6–Comparison of different concrete input parameters

Fig. 7–Unconfined uniaxial stress-strain curve of concrete based on CSCM

Fig. 8–Comparison of load-displacement curves between test and FE model

Fig. 9–Comparison of failure modes between test and FE model: (a) US [5]; (b) US-CL-1F

Fig. 10–Comparison of the crack distributions between test and FE model: (a) US [5]; (b) US-CL-1F

Fig. 11–Details of numerical model for load distribution rig

Fig. 12–Layout of the loading system (unit: mm)

Fig. 13–Numerical model of US-UDL-1F

Fig. 14–Comparison of load-displacement curves between US-CL-1F and US-UDL-1F

Fig. 15–Failure modes of the slab in model US-UDL-1F: (a) Top surface of the slab; (b) Bottom surface of the slab

Fig. 16–Development of beam axial force: (a) US-CL-1F; (b) US-UDL-1F

Fig. 17–Contribution of each supporting column: (a) US-CL-1F; (b) US-UDL-1F

Fig. 18–Dynamic resistance of beam-slab substructures

Fig. 19–Numerical models: (a) US-CL-2F; (b) US-UDL-2F

Fig. 20–Comparison of load-displacement curves between CL and UDL conditions

Fig. 21–Development of shear force of corner column

Fig. 22–Comparison of load resistance from different stories with single-story substructure: (a) US-CL-2F; (b) US-UDL-2F

Fig. 23–Load resistance of each story under CL: (a) US-CL-3F; (b) US-CL-4F; (c) US-CL-5F

Fig. 24–Load resistance of each story under UDL: (a) US-UDL-3F; (b) US-UDL-4F

Fig. 25–Beam axial force of each story under CL: (a) US-CL-3F; (b) US-CL-4F; (c) US-CL-5F

Fig. 26–Beam axial force of each story under UDL: (a) US-UDL-3F; (b) US-UDL-4F

Table 1-Reinforcement properties

Items	Diameter (mm)	Yield strength (MPa)	Ultimate strength (MPa)	Elongation (%)	Yield strain (με)
R6	6	324	525	23	1543
T12	12	427	530	18	2135

Note: R6 represents plain bar with diameter of 6 mm; T12 represents deformed rebar with diameter of 12 mm.

Table 2-Study on different mesh sizes

Type	**Mesh size 1**	**Mesh size 2**	**Mesh size 3**
Mesh size of slabs (mm)	25×25×23.3	20×20×17.5	20×20×14
Mesh size of beams and columns (mm)	25×25×25	20×20×20	15×15×15
Mesh size of Reinforcements (mm)	25	20	15
Total number of solid elements	76672	152325	367990
Total number of beam elements	23330	29210	38708
Time consuming (s)	36241	43717	144940

Table 3-Model parameters of CSCM for FE models (Unit: N, mm and ms)

MID	**RO**	**NPLOT**	**INCRE**	**IRATE**	**ERODE**	**RECOV**	**ITRETRE**
1	0.00232	1	0.0	0	1.10	0.0	0
PRED							
0.0							
G	**K**	**ALPHA**	**THETA**	**LAMDA**	**BETA**	**HN**	**CH**
5000	5476	13.408	0.2751	10.5	0.01929	0.0	0.0
ALPHA1	**THETA1**	**LAMDA1**	**BETA1**	**ALPHA2**	**THETA2**	**LAMDA2**	**BETA2**
0.74735	0.001315	0.17	0.07639	0.66	0.001581	0.16	0.07639
R	**XD**	**W**	**D1**	**D2**			
5.0	87.8	0.05	2.5e-4	3.492e-7			
B	**GFC**	**D**	**GFT**	**GFS**	**PWRC**	**PWRT**	**PMOD**
100.0	3.308	0.1	0.06616	0.03308	5.0	1.0	0.0
ETA0C	**NC**	**ETAOT**	**NT**	**OVERC**	**OVERT**	**SRATE**	**REP0W**
0.0	0.0	0.0	0.0	0.0	0.0	0.0	0.0

Table 4-Comparison of key results between test and FE model

Results Source	Critical Displacement (mm)		Critical Load (kN)		
	YL	PL	YL	PL	UL
Test	50	85.2	35	43.5	14.1
FEM	46.8	83.6	37.1	43.7	13.6
FEM/Test	0.936	0.981	1.06	1.005	0.965

Note: YL, PL, and UL represent yield load, peak load, and ultimate load, respectively.

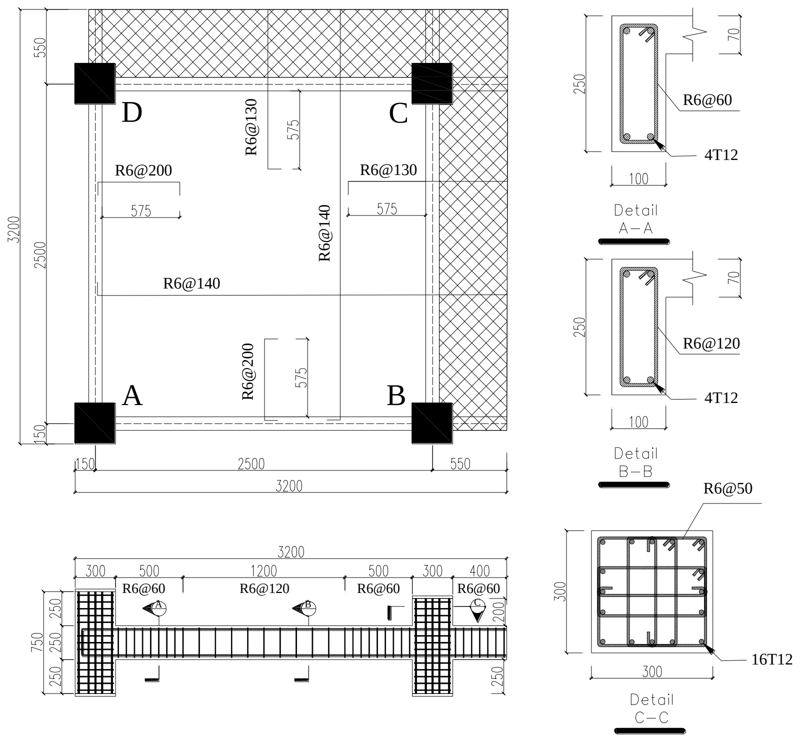

Fig. 1 Dimensions of Specimen US (units: mm) [5]

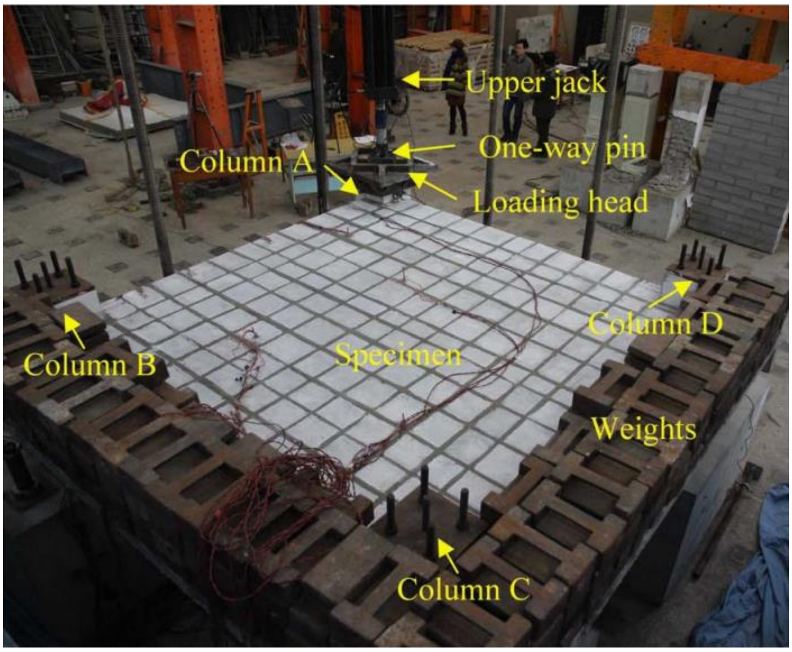

Fig. 2 Test setup and instrumentation location in the referenced experiment [5]

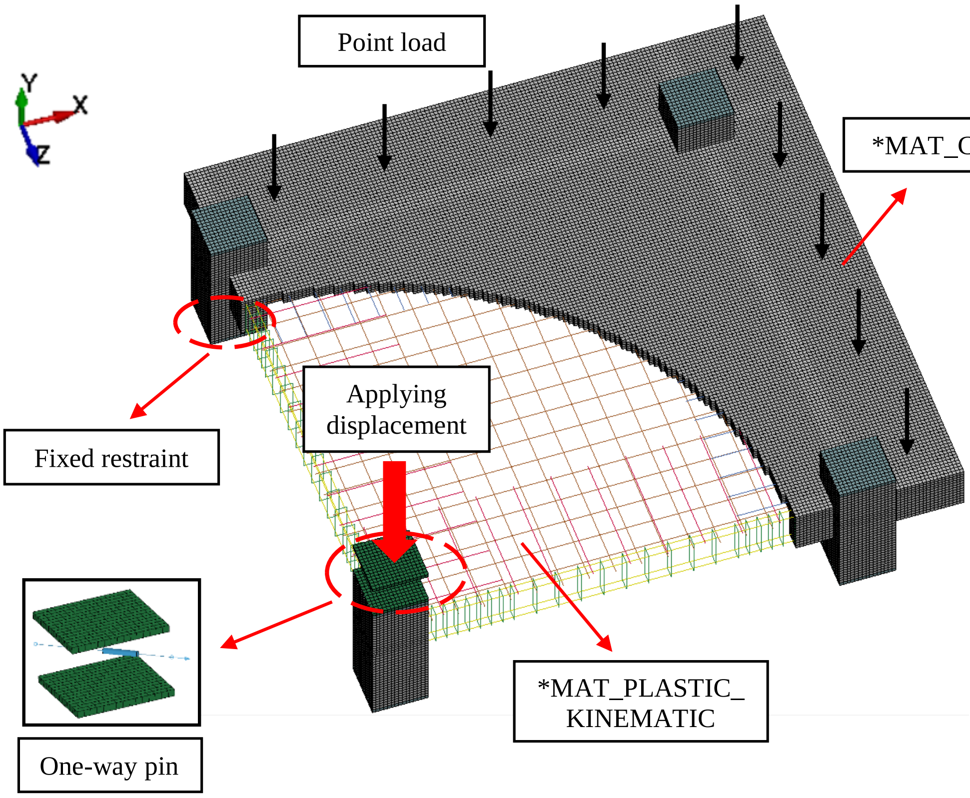

Fig. 3 Numerical model of US-CL-1F

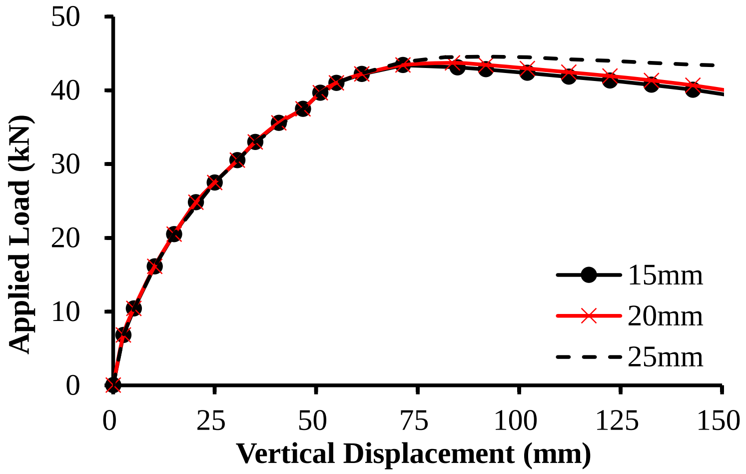

Fig. 4 Comparison of different mesh sizes

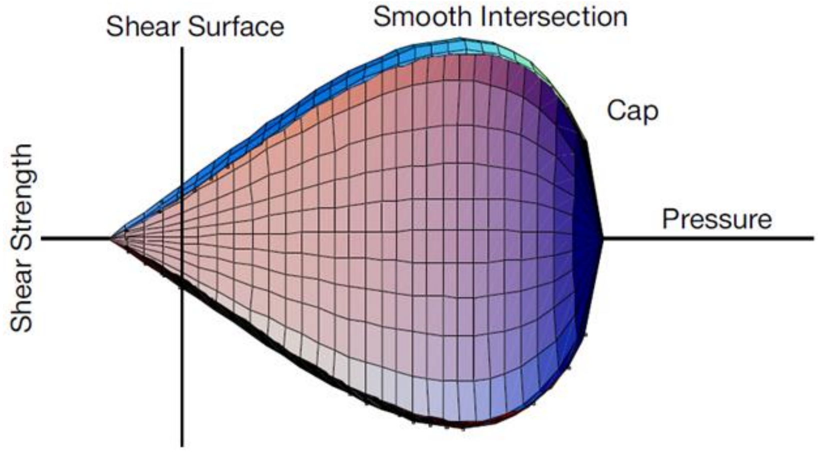

Fig. 5 General shape of concrete model yield surface

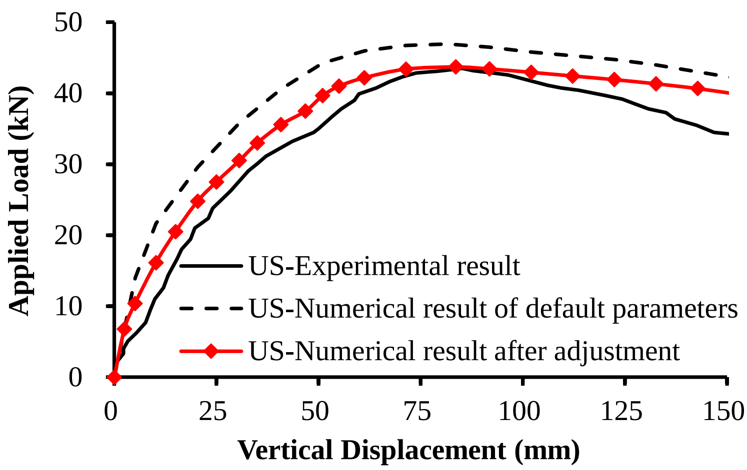

Fig. 6 Comparison of different concrete input parameters

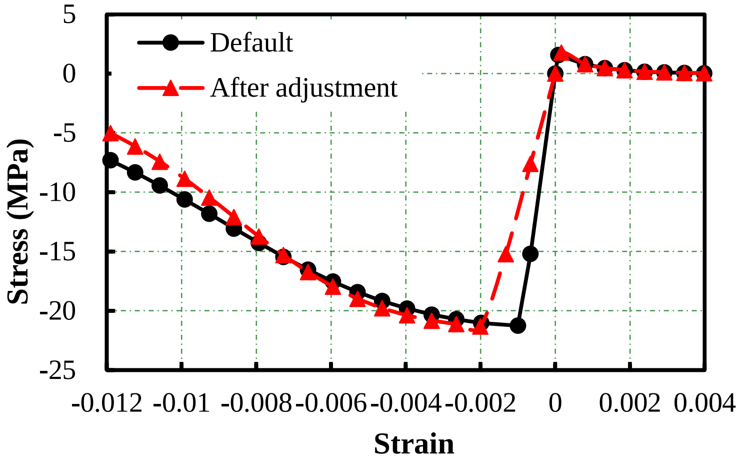

Fig. 7 Unconfined uniaxial stress-strain curve of concrete based on CSCM

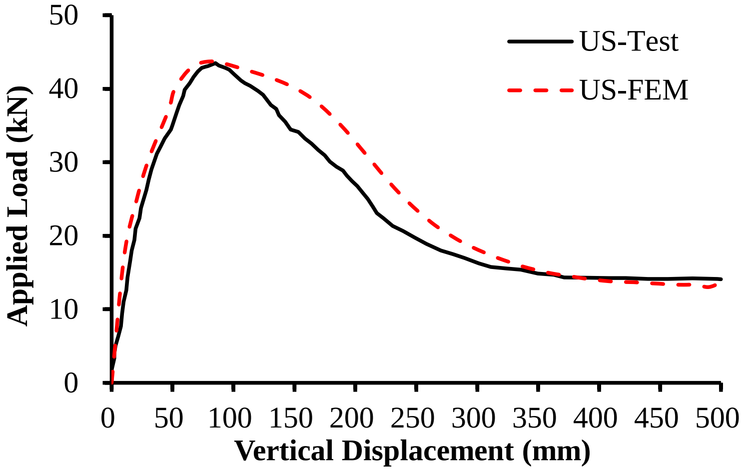

Fig. 8 Comparison of load-displacement curves between test and FE model

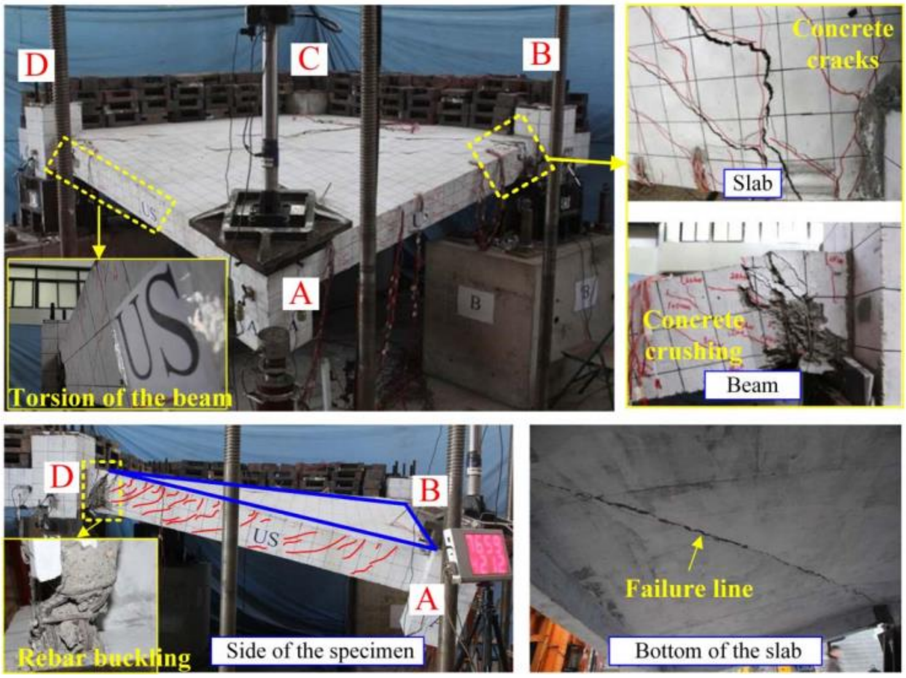

(a)

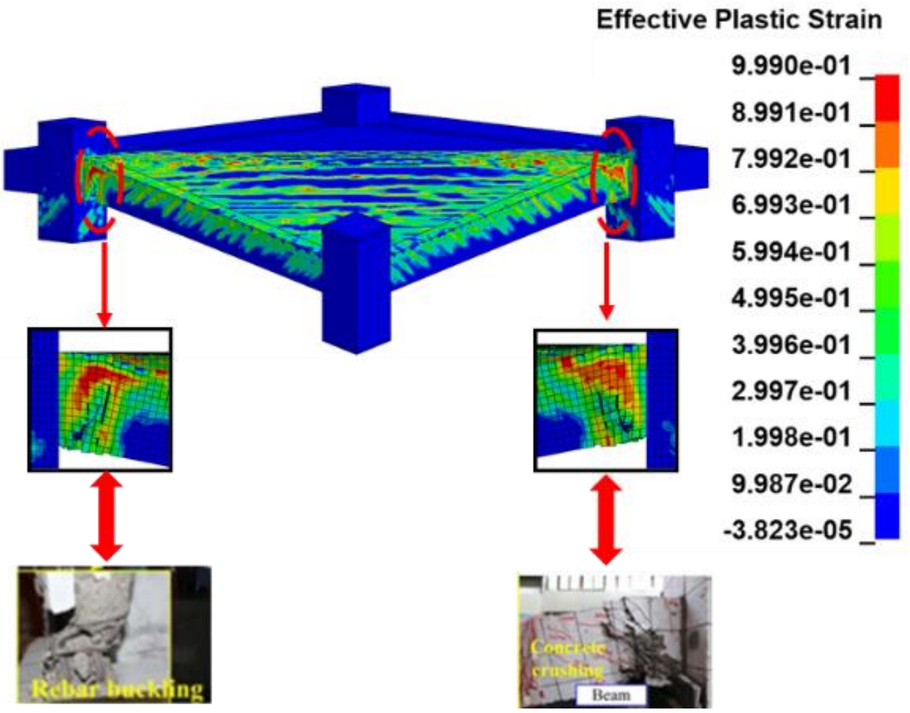

(b)

Fig. 9 Comparison of failure modes between test and FE model: (a) US [5]; (b) US-CL-1F

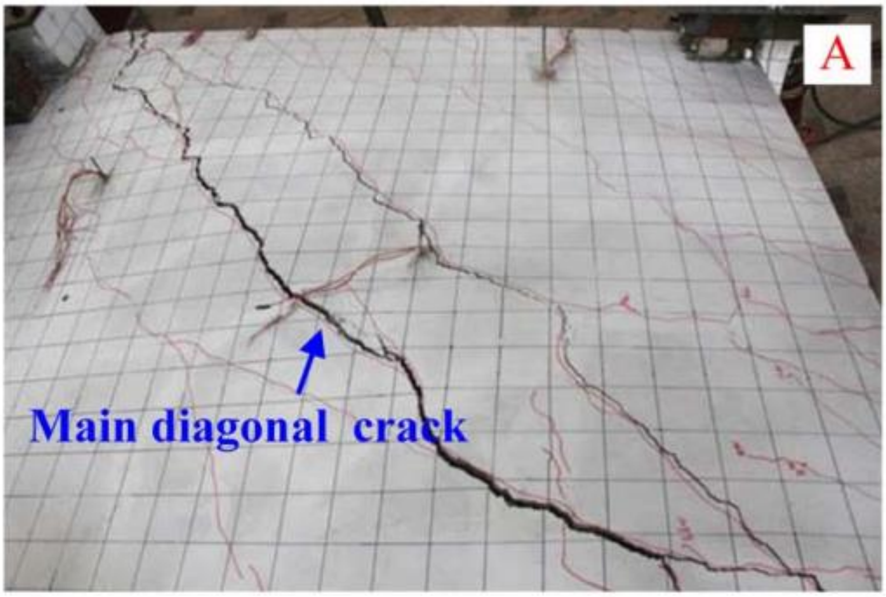

(a)

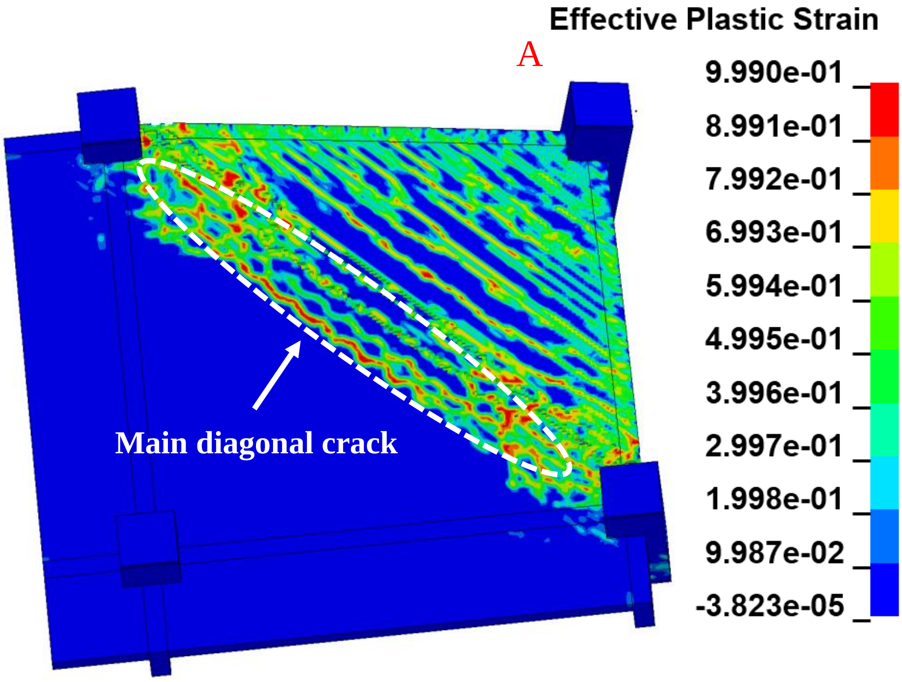

(b)

Fig. 10 Comparison of the crack distributions between test and FE model: (a) US [5]; (b) US-CL-1F

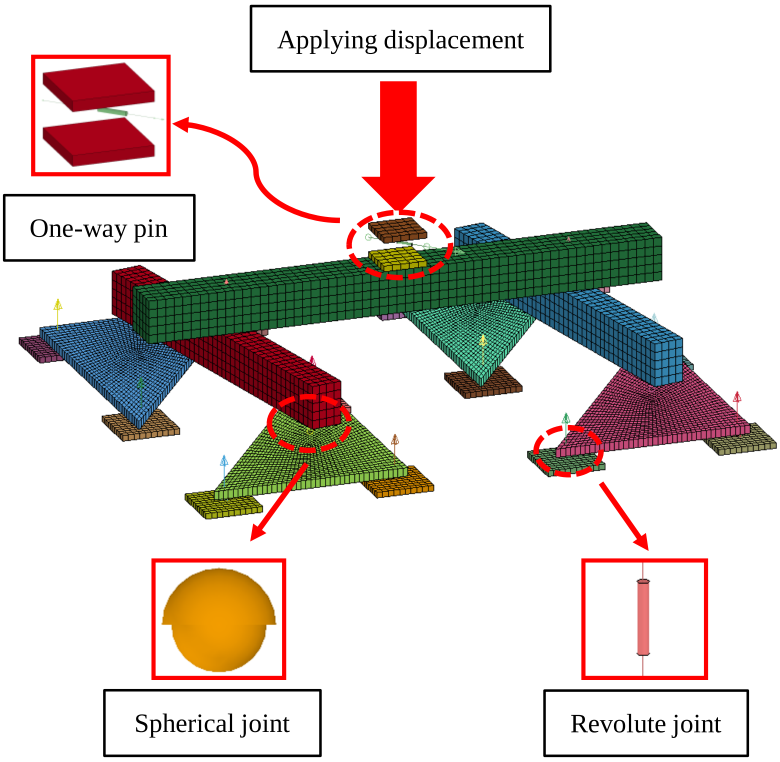

Fig. 11 Details of numerical model for load distribution rig

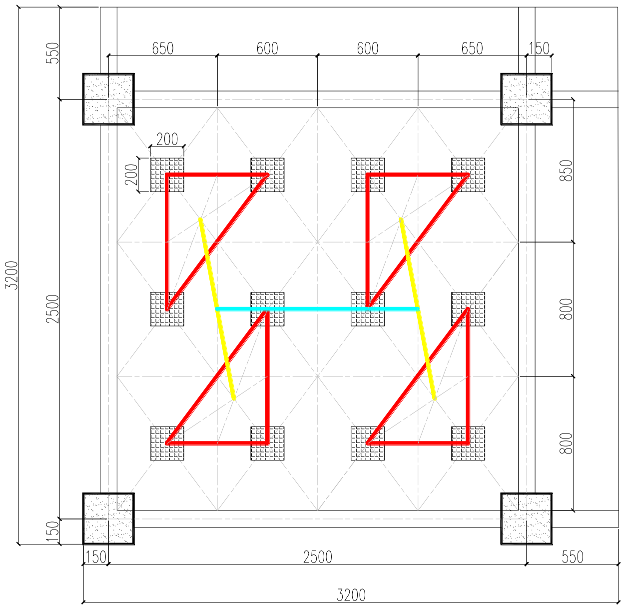

Fig. 12 Layout of the loading system (unit: mm)

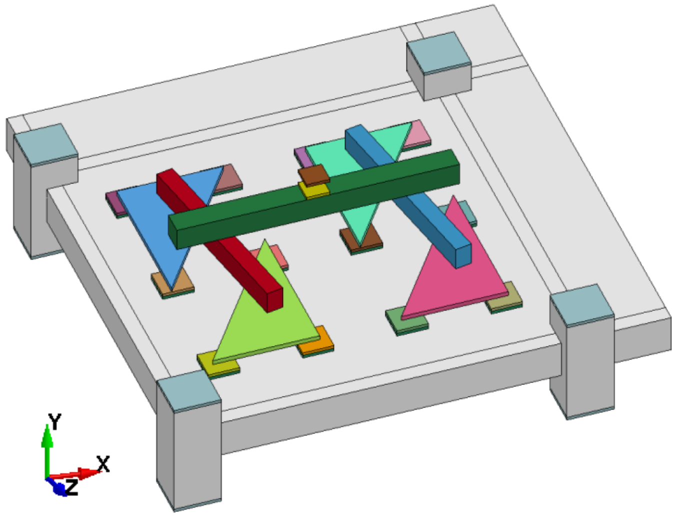

Fig. 13 Numerical model of US-UDL-1F

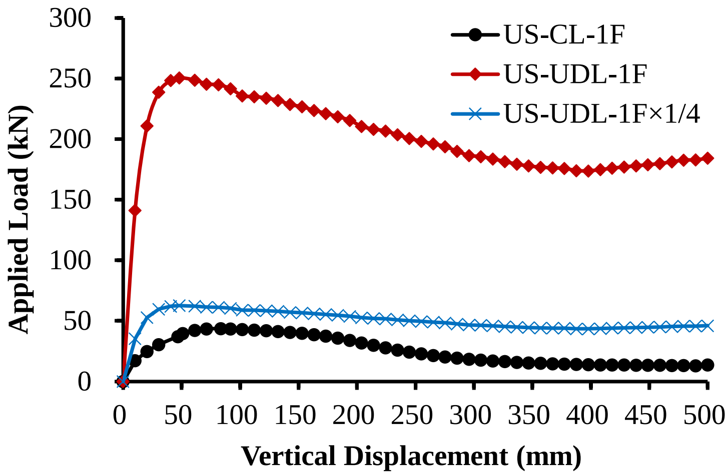

Fig. 14 Comparison of load-displacement curves between US-CL-1F and US-UDL-1F

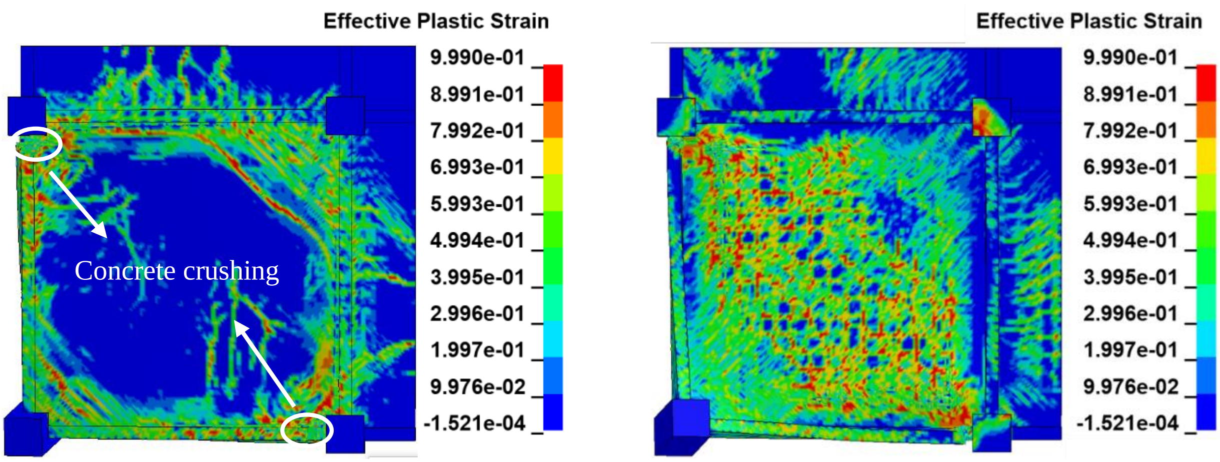

(a) (b)

Fig. 15 Failure modes of the slab in model US-UDL-1F: (a) Top surface of the slab; (b) Bottom surface of the slab

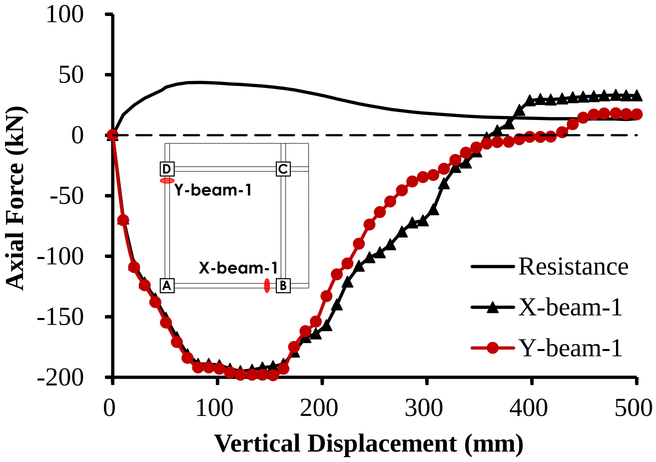

(a)

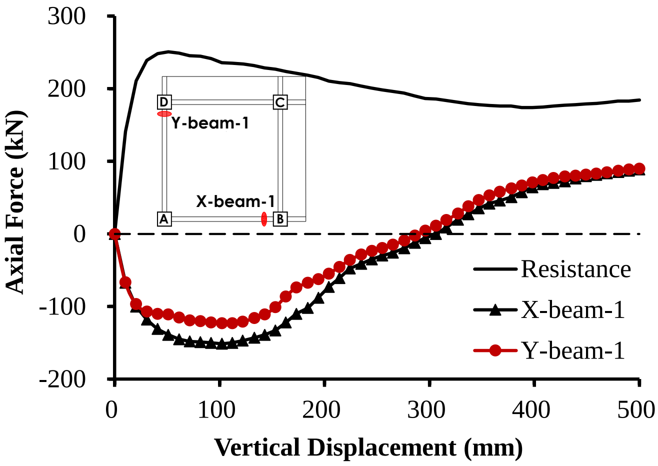

(b)

Fig. 16 Development of beam axial force: (a) US-CL-1F; (b) US-UDL-1F

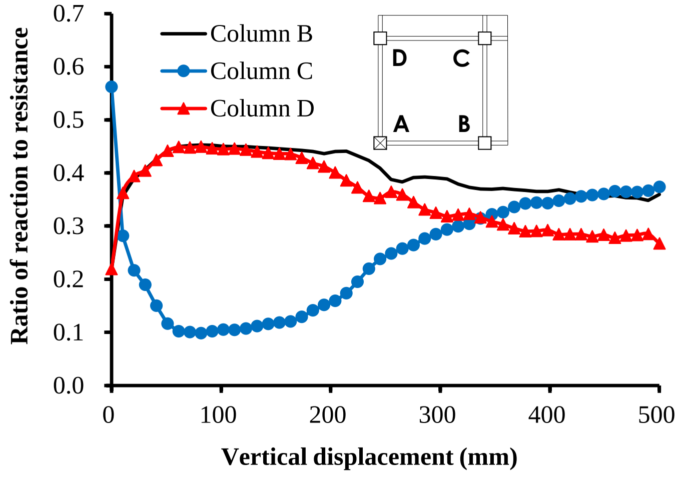

(a)

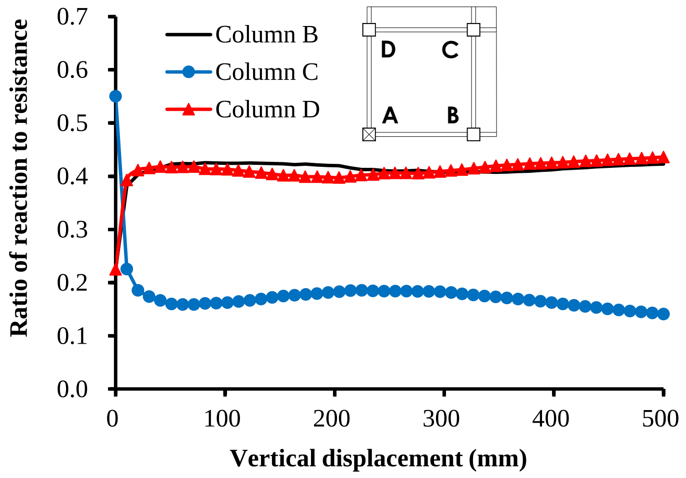

(b)

Fig. 17 Contribution of each supporting column: (a) US-CL-1F; (b) US-UDL-1F

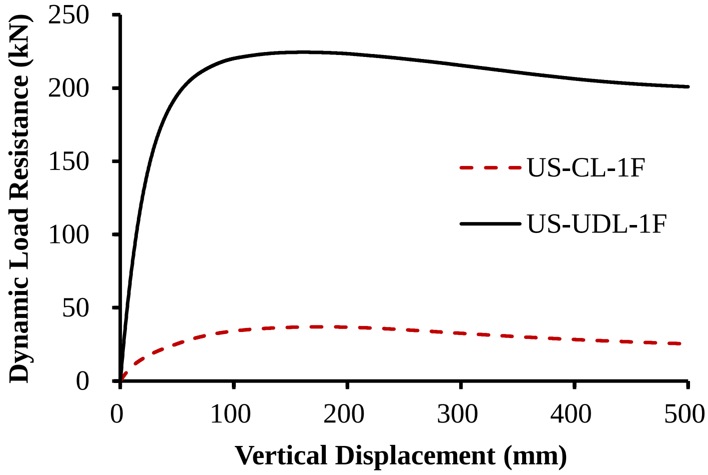

Fig. 18 Dynamic resistance of beam-slab substructures

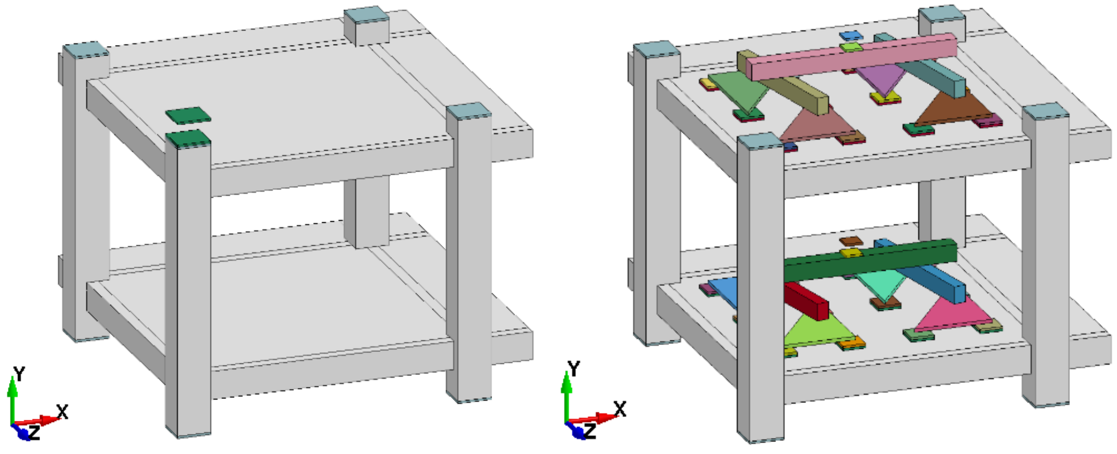

(a) (b)

Fig. 19 Numerical models: (a) US-CL-2F; (b) US-UDL-2F

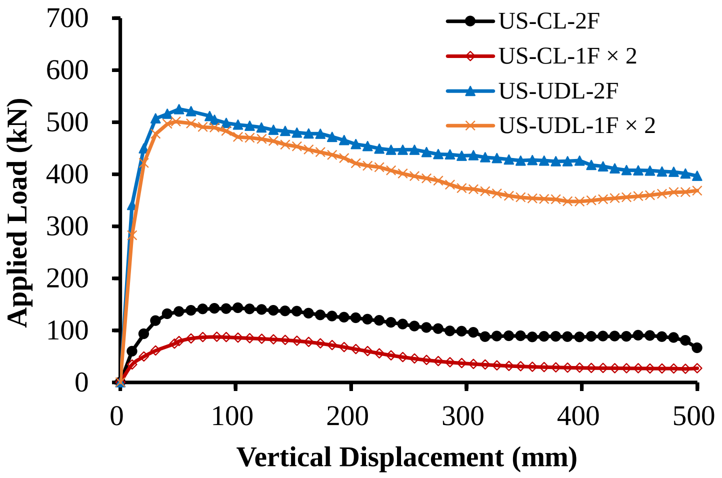

Fig. 20 Comparison of load-displacement curves between CL and UDL conditions

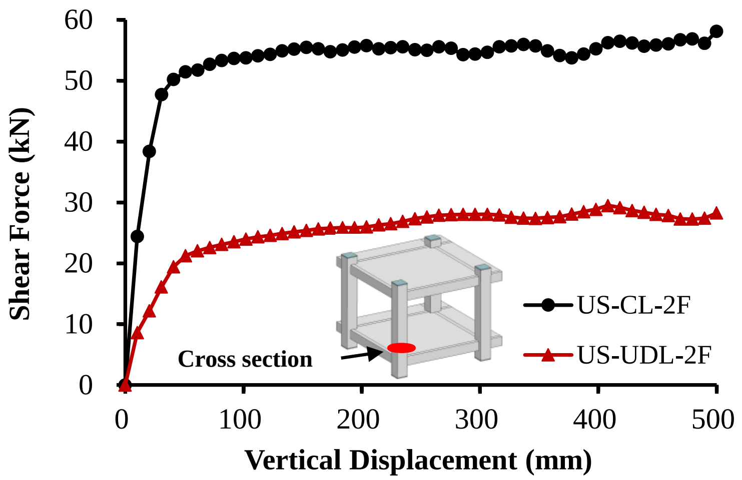

Fig. 21 Development of shear force of corner column

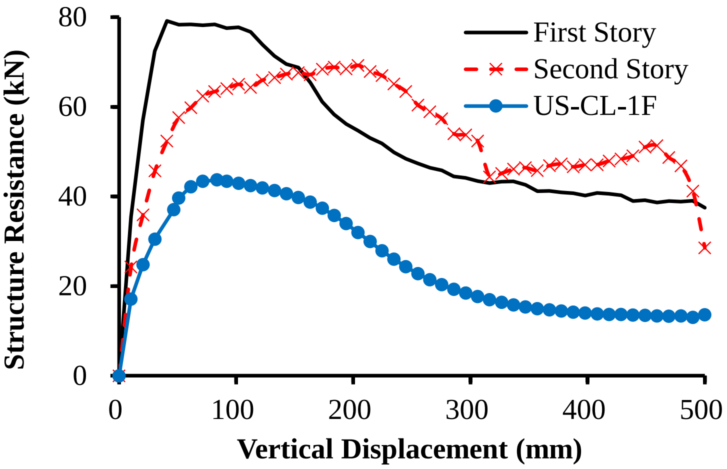

(a)

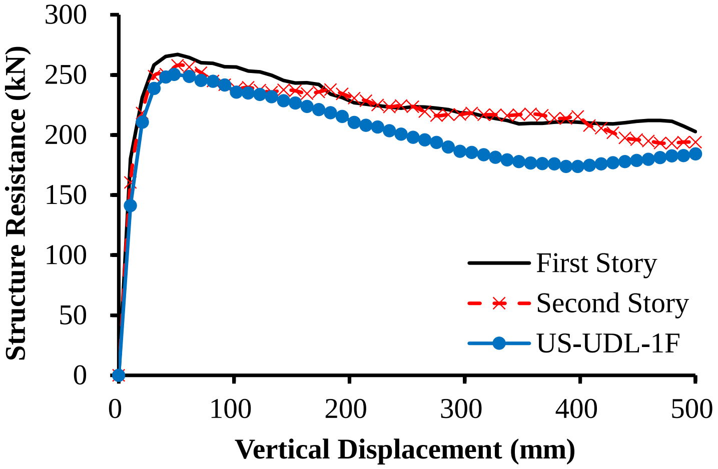

(b)

Fig. 22 Comparison of load resistance from different stories with single-story substructure:

(a) US-CL-2F; (b) US-UDL-2F

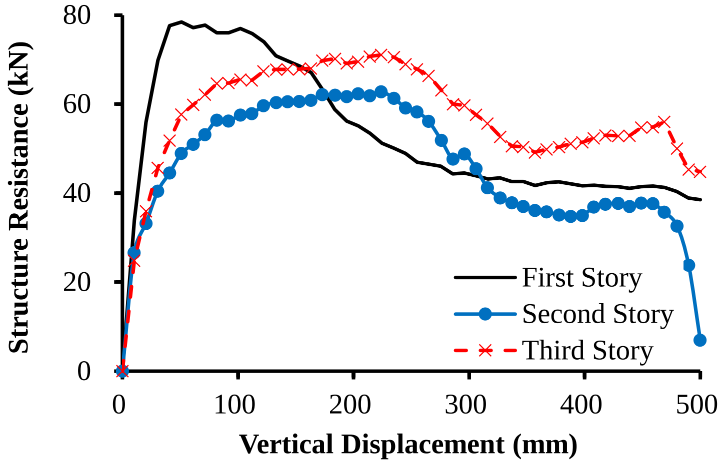

(a)

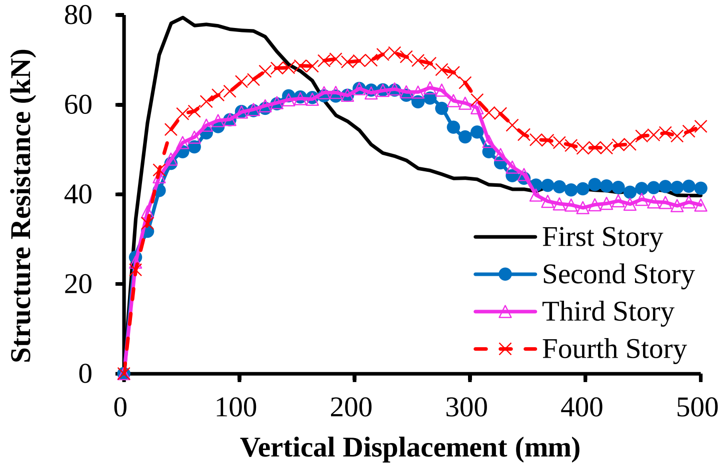

(b)

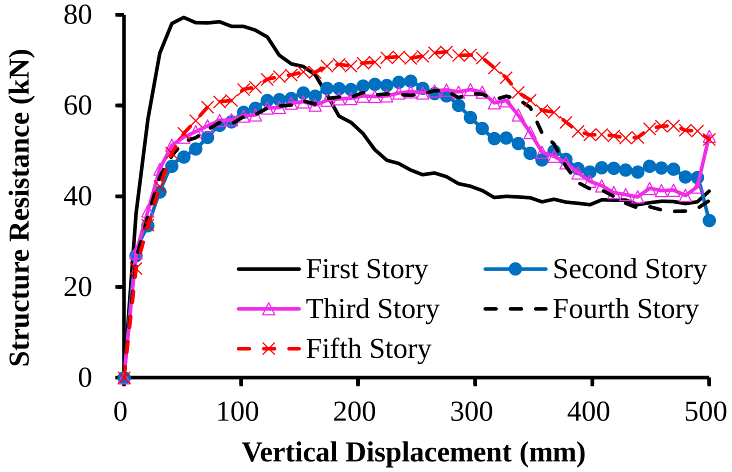

(c)

Fig. 23 Load resistance of each story under CL: (a) US-CL-3F; (b) US-CL-4F; (c) US-CL-5F

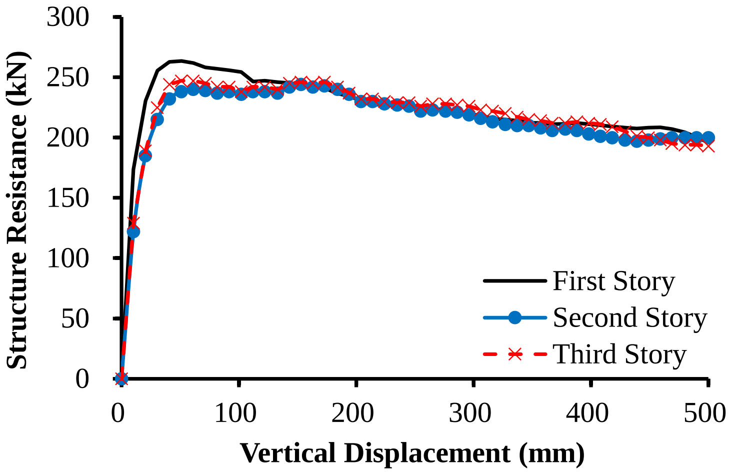

(a)

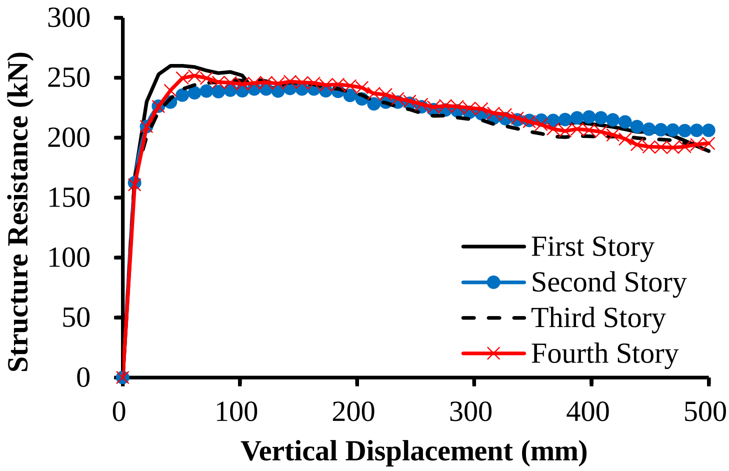

(b)

Fig. 24 Load resistance of each story under UDL: (a) US-UDL-3F; (b) US-UDL-4F

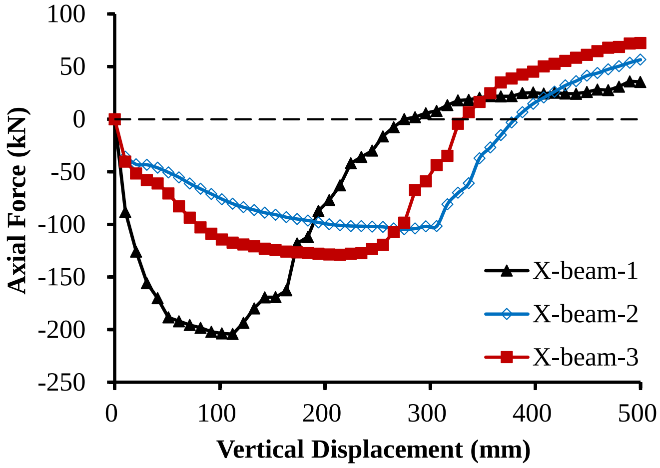

(a)

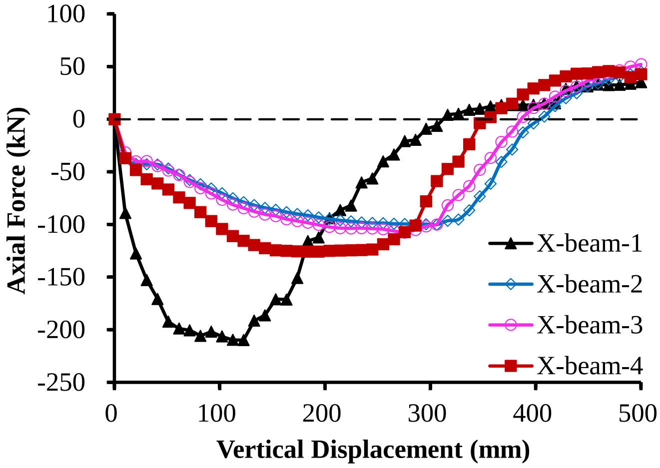

(b)

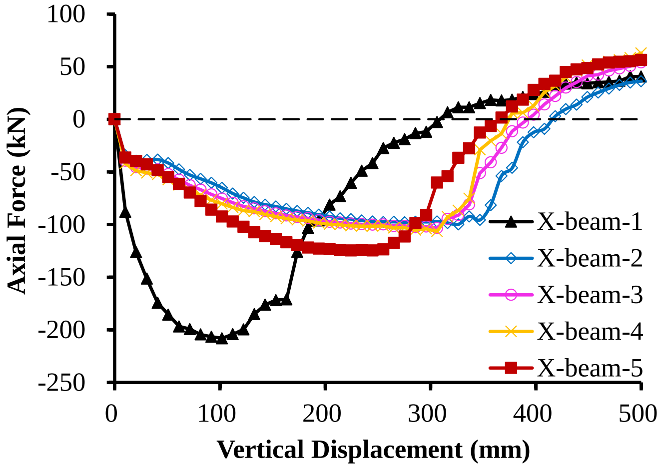

(c)

Fig. 25 Beam axial force of each story under CL: (a) US-CL-3F; (b) US-CL-4F; (c) US-CL-5F

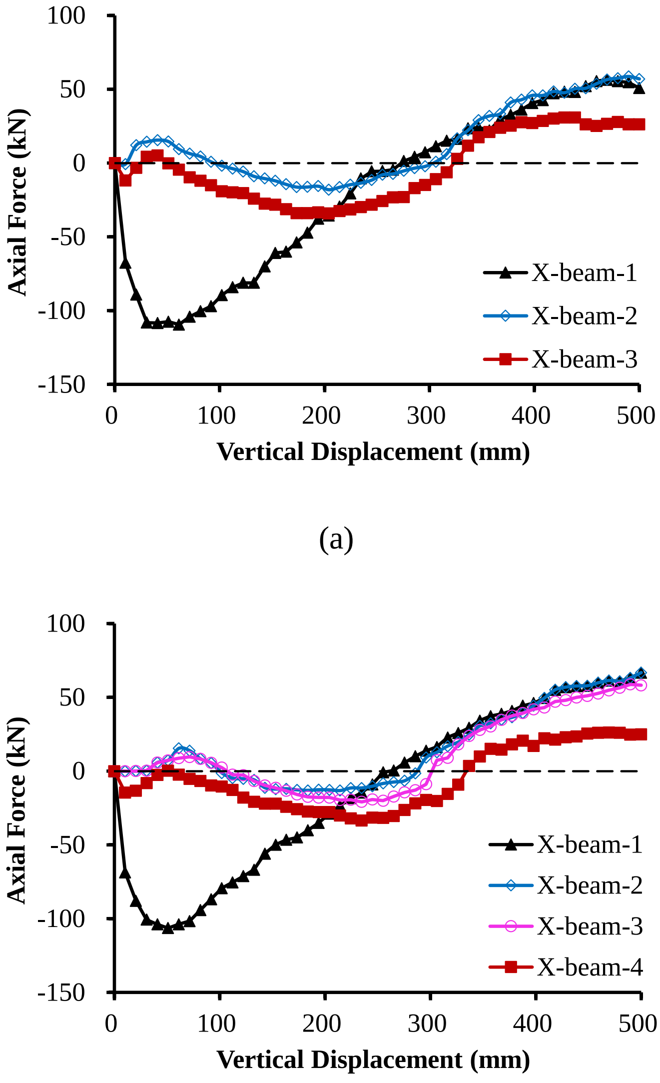

(a)

(b)

Fig. 26 Beam axial force of each story under UDL: (a) US-UDL-3F; (b) US-UDL-4F

Dear Editor

This manuscript has no conflict of interest.

Please contact with the corresponding author (Kai Qian) by E-mail: qiankai@ntu.edu.cn, if necessary. Thank you so much!

Regards
Kai Qian

Author Statements

Kai Qian: Conceptualization. **Jian-Fei Cheng:** Methodology and Formal Analysis. **Yun-Hao Weng**: Writing- Original Draft Preparation. **Feng FU**: Writing- Original Draft Preparation.

Effect of Loading Methods on Progressive Collapse Behavior of RC Beam-Slab Substructures under Corner Column Removal Scenario

Kai Qian[1,2*], Jian-Fei Cheng[1], Yun-Hao Weng[1], Feng Fu[3]

[1]College of Civil Engineering and Architecture, Guangxi University, Nanning, China, 530004.

[2]College of Civil Engineering and Architecture, Guilin University of Technology, Guilin, China, 541004.

[3]School of Mathematics, Computer Science and Engineering, City, University of London, U.K, EC1V 0HB.

Abstract: In this paper, high-fidelity finite element (FE) models were developed to investigate the behavior of reinforced concrete (RC) beam-slab substructures to resist progressive collapse under a corner column removal scenario. The numerical models were validated by test results. Then, the validated FE models were employed to investigate the structural behavior under different loading methods, including concentrated loading (CL) and uniformly distributed loading (UDL) methods. Moreover, multi-story frames were built to capture the load redistribution behavior of substructures at different floors under different loading methods. The results indicated that the loading methods affect overall structural responses, load transfer mechanisms, and failure modes. It was demonstrated that the Vierendeel action could not be ignored for multi-story frames to resist progressive collapse caused by the loss of a corner column scenario. More significant Vierendeel action was developed in the structure subjected to CL method than that subjected to UDL method. It was also found that the load transfer mechanisms developed in the top story and bottom story for a multi-story frame are pretty different from those in the middle stories. The bottom story has the most remarkable load resisting capacity.

Keywords: Progressive collapse; Loading method; Load transfer mechanism; Corner column removal.

* Corresponding author. E-mail address: qiankai@glut.edu.cn

1. Introduction

ASCE/SEI-10 (2010) [1] defines progressive collapse as the spread of an initial local failure from element to element, eventually resulting in the collapse of the entire structure or a large part of it disproportionately. Progressive collapse first attracted public attention after the partial collapse of Ronan Point apartment in London. The research topic became popular after the collapse of Alfred P. Murrah Federal Building in Oklahoma City and World Trade Center in New York. To date, several codes and design guidelines (ASCE/SEI-10 2010 [1]; General Services Administration (GSA) 2003 [2]; Department of Defense (DoD) 2009 [3]) had been issued for practical engineers to design buildings in mitigating progressive collapse. There are two main methods commonly suggested by design guidelines: direct and indirect design methods. Due to the uncertainty of extreme events, the alternate load path (ALP) method, one of the direct design methods, has been considered as a major technique as it is event-independent.

In the past decades, numerous experimental studies [4-18] and numerical simulations [19-25] have been conducted to investigate the progressive collapse behavior of reinforced concrete (RC) and precast concrete (PC) structures based on the ALP method. Remarkable efforts have been made towards deeper understanding of load transfer mechanisms, such as compressive arch action (CAA) [4-6], tensile catenary action (TCA) [7-9] developed in beams, and compressive membrane action (CMA) [11,12], tensile membrane action (TMA) in slabs [20,21]. Zhou et al. [4] conducted a series of static tests on a one-third scaled RC specimen and two PC specimens using dowel bars and corbel to investigate the load transfer mechanisms of these specimens under a middle column loss. Feng et al. [5] investigated the progressive collapse behavior of four beam-slab substructures subjected to a corner column loss. It was found that the development of TCA was limited due to weak horizontal constraints from the surrounding elements. Sasani [6] investigated the dynamic response of a 6-story RC frame subjected to simultaneous removal of a corner column and an adjacent exterior column. They concluded that the three-dimensional Vierendeel action plays a key role in load redistribution. It should be noted that the maximum vertical displacement was so low that no CAA and TCA were developed. Lu et al. [9] and Ren et al. [10] conducted several series of laboratory tests on RC specimens with or without slabs. In their tests, both the middle and edge column removal scenarios were investigated. It was found that the effects of beam height, slab thickness, and seismic reinforcing details dominate the progressive collapse resistance of RC frames.

It should be noted that the majority of existing tests relied on the concentrated loading (CL) method, which applied a concentrated load on the removed column. However, in reality, the load was uniformly distributed on the slab or beam. Thus, the uniformly distributed loading (UDL) method should be applied to represent real load patterns. However, for UDL method, the weights were increased slowly to simulate the increment of UDL, which should be very dangerous when reached the ultimate load capacity. In addition, the softening branch of the load-displacement curve could not be captured. To overcome this drawback, as an alternative method, the multi-points loading method (equivalent UDL), which was a displacement-controlled method, was widely adopted in previous investigations [15-19,21]. Qian et al. [15] carried out a series of RC beam-slab substructures under different column missing scenarios. The UDL method was equivalently applied on the slab by a specially designed loading frame. Pham et al. [17] also adopted the loading tree to equivalently apply UDL on progressive collapse performance of beam-slab substructures under the loss of an exterior column scenario. Moreover, flat slab or flat plate substructures were tested under the equivalent UDL method to investigate the effects of loading methods subjected to an interior column removal scenario [16,19].

The effects of loading methods on performance of RC substructures have been explored [18, 21]. The influence of loading methods on the behavior of buildings subjected to the loss of a corner column is still unclear due to insufficient investigations. Moreover, previous investigation was focused on single-story substructures [5,13], which has to ignore the Vierendeel action, one of the important load resisting mechanisms for RC frames subjected to the loss of a corner column scenario. Thus, in this study, high fidelity finite element (FE) models were developed to quantify the effects of different loading methods on the performance of RC frames to resist progressive collapse caused by the loss of a corner column scenario. Furthermore, multi-story frames were built to investigate the efficiency of Vierendeel action and quantify the mobilization of load transfer mechanisms among different stories with various loading methods.

2. Experimental program and numerical validation

2.1. Brief of the experimental program

Before conducting this numerical study, the FE model was validated by the experimental results of Feng et al. [5]. The experimental program [5] will be introduced briefly for readers easy to understand the validation and FE models. A seismically designed 6-story RC prototype building was designed following Chinese codes [26,27], with a height of 3900 mm in the first story and 3600 mm in upper stories. The span length in both directions was 5000 mm. The dead load (DL) and live load (LL) were 5.5 and 2.0 kPa, respectively. Four 1/2 scaled RC beam-slab substructures were tested subjected to the loss of a corner column scenario. However, only the results of Specimen US from Feng et al. [5] were used for validation in this study. The dimensions and reinforcement details of Specimen US are shown in Fig. 1. The overall dimension was 3200 mm × 3200 mm. The cross-section of the beam and column was 100 mm × 250 mm and 300 mm × 300 mm, respectively. The slab thickness was 70 mm. The transverse reinforcement was bent up 135° and was also installed in the beam-column joints in accordance with seismic RC detailing. The typical experimental setup and instrumentations are shown in Fig. 2. Three column supports were fixed to the RC blocks, which were fixed to the strong floor by bolts. To simulate the additional constraints from the surrounding slabs, a uniformly distributed load of 12.0 kN/m^2 was applied on the extending part of the slab. The load combination of (2DL+0.5LL) is selected, as suggested by GSA 2003 [2]. It should be noted that a one-way pin was installed between the hydraulic jack and the top of the corner column stub to allow the corner column stub to rotate and to ensure no extra bending will be introduced in the loading process. Thus, Vierendeel action of the frames can be neglected in this experimental program. A displacement-controlled CL manner was adopted.

The average cubic compressive strength of the concrete of Specimen US was 26.6 MPa, which corresponded to the cylinder compressive strength of 21.3 MPa. The measured reinforcement properties are tabulated in Table 1. For detail of test results, please refer to Feng et al. [5].

2.2. Numerical model setup

Commercial software LS-DYNA was adopted in this numerical study. Explicit solver was adopted to avoid divergence problems. The geometric model of Specimen US is shown in Fig. 3. Similar geometric dimensions, reinforcement details, and boundary conditions to the experimental test [5] were used in this numerical model.

2.2.1. Element types

As shown in Fig. 3, both concrete and steel plates were simulated by 8-node solid elements with a reducing integration scheme. There was one integration point in each solid element, which can considerably save computational time on the premise of accuracy when hourglass control is appropriately defined. To ensure the hourglass energy was less than 10% of the total internal energy, the hourglass coefficient was determined as 0.001. Flanagan-Belytschko stiffness form with exact volume integration was used. Moreover, reinforcements were modeled using 2-node Hughes-Liu beam elements with 2×2 Gauss quadrature integration. This beam formulation could effectively simulate the mechanical property of reinforcements, such as axial force, bi-axial bending, and transverse shear strain.

In this study, sensitivity analysis with three different mesh sizes of 25 mm, 20 mm, and 15 mm are conducted, as tabulated in Table 2. As shown in Fig. 4, mesh size of 20 mm is adequate, as further mesh refinement will not further enhance the accuracy significantly. As a result, the mesh size of concrete element is chosen as 20 mm × 20 mm × 17.5 mm for RC slabs and 20 mm × 20 mm × 20 mm for other components. The size of beam element is 20 mm.

2.2.2. Material model

Several constitutive models are available in the material library of LS-DYNA. In this study, continuous surface cap model (CSCM) is used for concrete as it could effectively simulate the mechanical property of concrete, including damage–based softening, modulus reduction, shear dilation, shear compaction, confinement effect, and strain rate effect [28]. The failure of CSCM model is controlled by the shear failure surface and hardening cap surface [29], as shown in Fig. 5. And the yield surface is formed based on three stress invariants J_1, J'_2, and J'_3. Previous studies [19-23] found that erosion criterion based on the maximum principal strain is a suitable way to simulate concrete crushing or spalling under both quasi-static and dynamic conditions. However, it could not simulate shear failure well when only the maximum principal strain was adopted for the definition of erosion criterion. Thus, Weng et al. [19] suggested that the maximum principal strain and shear strain criterions should be considered simultaneously by using keyword *Mat_Add_Erosion. Since the appropriate values are dependent on the mesh size, the value of maximum principal strain and shear strain is set to 0.08 and 0.3 based on multiple trials. Once the maximum principal strain or shear strain is reached, the solid element is deleted. Furthermore, the strain rate effect was ignored since only quasi-static behavior was discussed in this study.

LS-DYNA provides a simplified way to define CSCM (*Mat_CSCM_CONCRETE) for concrete properties, which only needs three input parameters (unconfined compressive strength $f_c^{'}$, maximum aggregate size A_g, and units). Then the remaining material properties are calculated automatically according to equations proposed by CEB-FIP concrete model code [30]. But the simplified CSCM is suited for $f_c^{'}$ between 28 MPa and 58 MPa. Since the unconfined compressive strength $f_c^{'}$ of Specimens US was 21.3 MPa, the original CSCM (*Mat_CSCM) is used, which requires a series of input parameters to define concrete material properties, as shown in Table 3.

However, the default concrete material properties would overestimate the initial stiffness and structural resistance, as shown in Fig. 6. Therefore, a few adjustments on the elasticity modulus and fracture energy of concrete were made to improve the numerical results. Previous studies [19-21,23] suggested that the tensile fracture energy G_{ft} could be reduced to 80% of the default one when it is over predicted. If shear or compressive-based damage is significant, the shear fracture energy G_{fs} should be set as $G_{fs} = 0.5G_{ft}$ and $G_{fc} = 50G_{ft}$. However, the default is $G_{fs} = 100G_{ft}$. In this study, since severe flexural and torsional failure occurred in the beam ends in Specimen US, both G_{ft} and G_{fs} were adjusted herein.

The detailed parameters of CSCM are listed in Table 3. The unconfined uniaxial stress-strain relationship of concrete after adjustments is shown in Fig. 7. The initial stiffness is lower than that of the default one, and the compressive stress reduces faster in the softening stage. As shown in Fig. 6, the adjusted material property could improve the numerical results significantly.

The symmetric bilinear elastic-plastic material model (*Mat_Plastic_Kinematic) is used for reinforcements, which assumes the tensile behavior is identical to that of compressive. The parameters of material properties, including elastic modulus, yield strength, tangential modulus, and ultimate strain, are determined based on the material tests. When the strain exceeds the ultimate elongation ratio, the corresponding reinforcement element is also deleted. The strain rate effect was ignored since only quasi-static behavior was discussed in this study. As suggested by previous works [19,23], a perfect bonding between concrete and reinforcement was assumed based on *Constrained_Lagrange_In_Solid.

2.2.3. Boundary conditions

In the numerical modeling, similar to the experimental program, the uniformly distributed load was applied on the extending area of the specimen. For simplicity, three concrete blocks were modeled using three rigid plates with zero translations and rotations, as indicated in Fig. 3. Furthermore, a rigid plate was generated at the top of the column stub to prevent stress concentration when concentrated loads were applied. Single surface (*Contact_Automatic_Single_Surface) was defined between the rigid plate and RC column. Besides, static and dynamic coefficients of friction were set as 1.0 at the contact surface to prevent any sliding of the rigid plate. Similar to experimental work, a one-way pin was generated between the loading plate and corner column by using constraint type *Constrained_Joint_Revolute.

2.3. Validation of the numerical model

Fig. 8 shows the comparison of load-displacement curves between the test results and FE model. At a large deformation, the TCA in beams and tensile membrane action in slabs is not efficiently mobilized due to the weak tie force from the surrounding structural members. Thus, the source of load resistance is mainly attributed to flexural action or beam action. As shown in Fig. 8, the load-displacement curve from FE model is quite similar to test results, including initial stiffness, yield load, ultimate load, and ultimate deformation capacity. The error of key results between the FE model and test one is less than 7 %, as listed in Table 4.

It is noted that the crack pattern of the RC beam-slab substructure cannot be directly demonstrated because concrete model CSCM is unable to track cracks. However, the cracks can be equivalently demonstrated by effective plastic strains. Generally, wider cracks expressed more significant effective plastic strains. The concrete damage was quantified through the damage index. Damage index of 0 and 1 represents no damage and complete failure, respectively. As shown in Figs. 9 and 10, FE model could effectively simulate concrete crushing or spalling of the beam and crack patterns of the slab.

As a result, the agreement of the load-displacement curves and the failure modes between the numerical and test results indicated the validity of the numerical model. Thus, the model was used to investigate the load transfer mechanisms of the RC frames with different loading methods and story numbers.

3. Effect of loading methods

Due to the limitation of cost and test conditions, only an experimental study under CL condition was conducted by Feng et al. [5]. However, UDL should be applied as gravity load and live load are uniformly distributed along the structure. Thus, it is necessary to study the difference between these two loading approaches. As a result, the validated FE model was utilized to evaluate the behavior of RC beam-slab substructures under both CL and UDL methods.

3.1. Details of UDL model

Previous studies [15-19,21] had proved the effectiveness of the 12-point loading tree to simulate the UDL scheme equivalently. Moreover, Weng et al. [19] modeled the load distribution rig with high fidelity, and the reliability of the numerical model was proved. Thus, in this study, the same modeling method was adopted to simulate the behavior of substructures under the UDL method. As shown in Fig. 11, the load distribution rig [19] consisted of a series of rigid beams and plates simulated by 8-node solid elements. The connection between the top and the secondary rigid beam was defined by keyword *Constrained_Joint_Revolute [19,21]. The connection between the secondary rigid beam and the triangle rigid plate was also modeled by keyword *Constrained_Joint_Revolute. The bottom steel plate was connected with the triangle steel plate by revolute joints to ensure the bottom plates could rotate. In addition, a contact function was used between the load distribution rig and RC frame by *Contact_Automatic_Single_Surface [19]. A one-way pin was also defined between the loading plate and the top rigid beam so that the top rigid beam was able to rotate around the one-way pin. In this study, each loading point coincided with the centroids of 12 sub-areas, as indicated in Fig. 12.

As shown in Fig. 13, a beam-slab substructure under the UDL method named US-UDL-1F was built based on the validated model of US-CL-1F. It should be noted that the dimensions, reinforcement details, and boundary conditions of US-UDL-1F are identical to those of US-CL-1F.

3.2. Structural resistance

Fig. 14 shows the comparison of the load-displacement curves from different loading schemes. As shown in the figure, the peak load of 43.7 kN and 250.6 kN was measured at US-CL-1F and US-UDL-1F, respectively. The initial stiffness, which is defined as the ratio of peak load to the corresponding displacement, of US-CL-1F and US-UDL-1F is 0.52 kN/mm and 5.2 kN/mm, respectively. Thus, the UDL method increases the peak load and initial stiffness by 473% and 897%, respectively. However, it should be noted that the load capacity from US-UDL-1F should be divided by four before comparing it with US-CL-1F based on a simple load distribution analysis. Thus, as shown in Fig. 14, the load-displacement curve of one-quarter of US-UDL-1F is generally more significant than that of US-CL-1F as the slab deformation of US-UDL-1F is more uniform. No major diagonal crack is formed, and more negative yield lines are observed at the top slab, as shown in Fig. 15.

3.3. Load redistribution of beam-slab substructures

To reveal the difference in load transfer mechanisms of the RC beam-slab substructures with different loading methods, the results of the internal forces of beams and columns were extracted. It should be noted that the beam sections are at a distance of 200 mm away from the beam-column interface to avoid element erosion and fail to provide the internal forces.

3.3.1. Development of axial force in beams

Fig. 16 shows the development of axial force at the cross-sections near the column stub. Due to symmetry, similar characteristics of axial force development are observed at cross-sections X-beam-1 and Y-beam-1. The axial force initially is compressive, indicating the mobilization of CAA. For CL and

UDL methods, when the displacement exceeds 370 mm and 296 mm, respectively, the axial force transfers into tension, reflecting the development of TCA.

The comparison between Fig. 16 (a) and (b) indicates that the UDL method significantly weakens the CAA of beams (e.g., the maximum axial compressive force reduces from 198.3 kN to 151.2 kN) but starts the TCA earlier and greater. For CL and UDL methods, the maximum axial tension force is 38.1 kN and 98.1 kN, respectively, which indicates that TCA is not efficiently mobilized due to fewer constraints from surrounding structural members.

3.3.2. Reactions of supporting columns

Figs. 17 (a) and (b) demonstrate the proportion of reaction force at different columns to the total reaction force under CL and UDL, respectively. For US-CL-1F, at the displacement of 50 mm, 44% and 44% of the load is distributed into columns B and D, respectively. Similarly, at this displacement stage, 42% and 42% of the load are distributed into columns B and D of US-UDL-1F. For US-CL-1F, after displacement of 82 mm, the proportion of columns B and D decreases with further increasing the displacement due to concrete crushing occurred at the beam AB and AD. Conversely, the proportion of column C keeps growing as column C remains almost intact during the test. However, for US-UDL-1F, after displacement of 20 mm, the proportion of columns B, C, and D nearly maintains constant because the deformation of the slab and beam is more uniform. In other words, column C suffers more significant damage when increasing the displacement.

3.4. Dynamic response

It is worth noting that progressive collapse is normally a dynamic event. Thus, it is necessary to evaluate the dynamic load capacity of the substructures under different loading methods. Based on previous studies [8,14,15,22], an energy-based model, which was proposed by Izzuddin et al. [31], was adopted in this dynamic evaluation. The dynamic resistance of the specimens could be determined by Eq. (1).

$$P_d(u_d) = \frac{1}{u_d}\int_0^{u_d} P_{NS}(u)du \tag{1}$$

where $P_d(u)$ and $P_{NS}(u)$ represent the dynamic load resisting function and nonlinear static load resisting function, respectively.

Fig. 18 illustrates the dynamic behavior of the beam-slab substructures. The dynamic peak loads of US-CL-1F and US-UDL-1F are 36.9 and 224.4 kN, respectively. Similar to the conclusions from nonlinear quasi-static results, the UDL method could increase the dynamic peak load by 508%. Even, the load resistance of US-UDL-1F is divided by four, the UDL method could increase the dynamic load capacity of CL-case by 52 %.

4. Analysis of multi-story frame structures

Progressive collapse is a global behavior for a multi-story building. However, only a single-story beam-slab substructure was tested in the test program [5]. Thus, it is imperative to understand whether the load transfer mechanisms in the single-story substructure are the same as those in a multi-story building. As shown in Fig. 19, US-CL-2F and US-UDL-2F were established, which represent a two-story frame substructure under CL and UDL methods, respectively. It should be noted that the load distribution tree, similar to US-UDL-1F, was generated in each story of US-UDL-2F.

4.1. The role of Vierendeel action

As concluded by Sasani [6], in moment frames, Vierendeel action is the major mechanism for the load redistribution of RC frames subjected to the loss of a corner column scenario. The Vierendeel action could resist the collapse of the buildings. For simplicity, due to the Vierendeel action, bending moment may develop in the beam end near the corner column to help the resistance of collapse.

Fig. 20 demonstrates the comparison of load resistance between single-story and two-story moment frames under both CL and UDL methods. The peak load of US-CL-1F, US-CL-2F, US-UDL-1F, and US-UDL-2F are 43.7 kN, 250.6 kN, 141.9 kN, and 525.2 kN, respectively. Thus, for CL method, the peak load of US-CL-2F is 324 % of that of US-CL-1F, which is much greater than the theoretical value of 200 %. The relatively large discrepancy could be attributed to Vierendeel action developed in US-CL-2F. For US-CL-1F, no Vierendeel action could be developed as the constraints from structural components in the upper story are ignored. However, the peak load of US-UDL-2F is 210 % of that of US-UDL-1F. Thus, comparing to CL method, the effects of Vierendeel action are quite limited. As mentioned above, the effects of Vierendeel action are expressed by developing positive moment at the beam end near the corner column. Thus, the mobilization of Vierendeel action may be reflected indirectly by the magnitude of shear force developed in the corner column. As shown in Fig. 21, much greater shear force develops in the corner column of US-CL-2F, comparing to US-UDL-2F.

4.2. Structural resistance from each story

Fig. 22 shows the comparison of the load resistance from different stories of a two-story frame with that from a single-story substructure. As shown in the figure, the load resistance of each story is different after the elastic stage. For CL method, compared with the single-story frame, the peak load of the first and second stories increases by 79 % and 58 %, respectively. However, under the UDL condition, the peak load of the first and second stories only increases by 7 % and 3 %, respectively. For both loading approaches, the bottom story achieves the greater load resisting capacity, which indicates that the Vierendeel action is more efficient in the bottom story, as the structural components in the second story could provide more significant constraints to the corner joint in the bottom story.

4.3. Load transfer mechanisms of multi-story RC frames

As aforementioned, the load transfer mechanisms in each story of the two-story frame are different. Thus, it is necessary to investigate load transfer mechanisms developing in each story of multi-story frames. Note that US-CL-3F, US-CL-4F, and US-CL-5F represent three-story, four-story, and five-story frame substructures under CL case, respectively. Similarly, US-UDL-3F and US-UDL-4F represent three-story and four-story frame substructures under the UDL case.

4.3.1. Structural resistance of multi-story frames

For US-CL-3F、US-CL-4F, and US-CL-5F, as shown in Fig. 23 (a), (b), and (c), the structural resistance developing in each story is different. The maximum load resistance is observed in the first story, which is the same as that found in US-CL-2F. By increasing the number of stories, it can be found that the initial stiffness, peak load, and residual load resistance of the middle story are pretty similar, which indicates that the development of load transfer mechanisms of the middle stories is almost identical. Moreover, the peak load of the middle stories is the least compared with the top and bottom ones. Like the CL case, for US-UDL-3F and US-UDL-4F, as shown in Fig. 24 (a) and (b), the bottom story also achieves the most significant initial stiffness and peak load. However, the difference of load resistance between the top story and the middle story is quite limited due to less Vierendeel action developed in UDL cases. In addition, due to the weak tie force from the surrounding elements, less TCA and TMA could be mobilized to resist progressive collapse under both CL and UDL methods. As shown in Fig. 23, comparing the load-displacement curve of the first story in models of US-CL-3F, US-CL-4F, and US-CL-5F shows that increasing the story number will not affect the load resistance and load transfer mechanisms of the first story. In other words, the constraints to the corner joint in the first story are similar whatever the story number is three, four, or five.

4.3.2. Axial force of beams in multi-story frames

Similar to what was discussed in section 3.3, the results of axial force in beams were also extracted to illustrate the load transfer mechanisms. For simplicity, only the cross-sections of beam AB were discussed herein. Note that the label of X-beam-1 to X-beam-5 represents the beams in the first to the fifth story, respectively.

As shown in Fig. 25, for CL case, the beams in each story are in compression before the displacement of 300 mm. After that, the axial force starts to decrease and changes into tension successively. Moreover, the beams in the first story begin to develop the CAA initially and achieve the maximum compressive force of 209.6 kN at the displacement of 112 mm. By contrast, beams in the top story achieve the maximum compressive force of 128.7 kN at the displacement of 214 mm, which indicates lower CAA developed in top story. Moreover, the compressive force is the least in the middle story compared with the top and first stories. Similarly, for UDL case, as shown in Fig. 26, the largest compressive force of 106.3 kN is measured in the first story. Moreover, the compressive force in the beams in the top story is slightly larger than that in the middle story.

For both loading methods, it is observed that the axial force of beams in the middle stories is similar, which agrees well with the results of load resistance.

5. Conclusions

Based on the numerical and parametric study conducted in this study, the following conclusions are drawn:

1. Compared with experimental results, it is found that the high-fidelity numerical models can simulate the global behavior of the RC beam-slab substructure subjected to a corner column loss scenario well. However, the shear fracture energy should be adjusted to well simulate the stiffness of the concrete in CSCM.

2. For single-story models under either UDL or CL methods: US-UDL-1F and US-CL-1F, the peak load of US-UDL-1F is 537 % of that US-CL-1F, which is greater than the theoretical value of 400%. Thus, it indicates that the simplified CL method may underestimate the load resistance of the beam-slab substructures subjected to the loss of a corner column scenario. It could be explained as UDL method may achieve more uniform deformation of the beam and slab, and thus, more materials could be fully mobilized.

3. For multi-story models, it was found that Vierendeel action could not be ignored to resist progressive collapse of RC frames caused by the loss of a corner column scenario. Comparing to multi-story frames subjected to UDL method, the Vierendeel action has more significant effects on the frames under CL method. As the building was subjected to UDL load, in reality, the commonly used CL method may overestimate the contribution of Vierendeel action. Moreover, the Vierendeel action is more efficient in lower stories than that in the upper stories. Therefore, in practical design, it was suggested to apply UDL load and generating multi-story frames to obtain more accurate results.

4. The numerical results indicated that the load transfer mechanisms developed in different stories are

not identical for a multi-story frame subjected to the loss of a corner column scenario. Moreover, it was found that increasing the story number will not affect the load resistance and load transfer mechanism of the first story.

References

[1] ASCE/SEI 7, Recommendations for Designing Collapse-Resistant Structures, Structural Engineering Institute-American Society of Civil Engineers, Reston, VA, 2010.

[2] GSA, Progressive Collapse Analysis and Design Guidelines for New Federal Office Buildings and Major Modernization Projects, U.S. General Service Administration, Washington, DC, 2003.

[3] Department of Defense (DoD), Design of Building to Resist Progressive Collapse. Unified Facility Criteria, UFC 4-023-03, US Department of Defense, Washington (DC), 2009.

[4] Y. Zhou, T.P. Chen, Y.L. Pei, H.J. Hwang, X. Hu, W.J. Yi, L. Deng, Static load test on progressive collapse resistance of fully assembled precast concrete frame structure, Eng. Struct. 200 (2019) 109719.

[5] P. Feng, H.L. Qiang, X. Ou, W.H Qin, J.X Yang, Progressive collapse resistance of GFRP-strengthened RC beam–slab subassemblages in a corner column–removal scenario, J. Compos. Constr. 23 (2018) 04018076.

[6] M. Sasani, Response of a reinforced concrete infilled-frame structure to removal of two adjacent columns, Eng. Struct. 30(9) (2008) 2478-2491.

[7] K. Qian, S.L. Liang, F. Fu, Y Li, Progressive collapse resistance of emulative precast concrete frames with various reinforcing details, J. Struct. Eng. 147(8) (2021) 04021107.

[8] X.F. Deng, S.L. Liang, F. Fu, K. Qian, Effects of high-strength concrete on progressive collapse resistance of reinforced concrete frame, J. Struct. Eng. 146(6) (2020) 04020078.

[9] X.Z. Lu, K.Q Lin, Y. Li, H. Guan, P.Q. Ren, Y.L. Zhou, Experimental investigation of RC beam-

slab substructures against progressive collapse subject to an edge-column-removal scenario, Eng. Struct. 149 (2017) 91-103.

[10] P.Q. Ren, Y. Li, X.Z. Lu, H. Guan, Y.L. Zhou, Experimental investigation of progressive collapse resistance of one-way reinforced concrete beam-slab substructures under a middle-column-removal scenario, Eng. Struct. 118 (2016) 28-40.

[11] N.S. Lim, K.H. Tan, C.K. Lee, Experimental studies of 3D RC substructures under exterior and corner column removal scenarios, Eng. Struct. 150 (2017) 409–427.

[12] A.T. Pham, N.S. Lim, K.H. Tan, Investigations of tensile membrane action in beam-slab systems under progressive collapse subject to different loading configurations and boundary conditions, Eng. Struct. 150 (2017) 520–536.

[13] K. Qian, B. Li, Slab effects on response of reinforced concrete substructures after loss of corner column, ACI Struct. J. 109 (6) (2012) 845–855.

[14] K. Qian, B. Li, J.X. Ma, Load-carrying mechanism to resist progressive collapse of RC buildings, J. Struct. Eng. 141(2) (2015) 04014107.

[15] K. Qian, B. Li, Z. Zhang, Influence of multicolumn removal on the behavior of RC floors, J. Struct. Eng. 142 (5) (2016), 04016006.

[16] K. Qian, B. Li, Load-resisting mechanism to mitigate progressive collapse of flat slab structures, Mag. Concr. Res. 67 (7) (2015) 349–363.

[17] P.X. Pham, K.H. Tan, Experimental response of beam-slab substructures subject to penultimate-external column removal, J. Struct. Eng. 141(7) (2015) 04014107.

[18] X.D. Pham, K.H. Tan, Experimental study of beam–slab substructures subjected to a penultimate-internal column loss, Eng. Struct. 55 (2013) 2–15.

[19] Y.H. Weng, K. Qian, F. Fu, Q. Fang, Numerical investigation on load redistribution capacity of flat slab substructures to resist progressive collapse, J. Build. Eng. 29 (2020) 101109.

[20] K. Qian, Y.H. Weng, F. Fu, X.F. Deng, Numerical evaluation of the reliability of using single-story substructures to study progressive collapse behaviour of multi-story RC frames, J. Build. Eng. 33 (2021) 101636.

[21] J. Yu, L. Luo, Y. Li, Numerical study of progressive collapse resistance of RC beam-slab substructures under perimeter column removal scenarios, Eng. Struct. 159 (2018) 14-27.

[22] A.T. Pham, K.H. Tan, J. Yu, Numerical investigations on static and dynamic responses of reinforced concrete sub-assemblages under progressive collapse, Eng. Struct. 149 (2017) 2-20.

[23] J. Yu, Y.P. Gan, J. Wu, H. Wu, Effect of concrete masonry infill walls on progressive collapse performance of reinforced concrete infilled frames, Eng. Struct. 191 (2019) 179-193.

[24] Y. Li, X.Z. Lu, H. Guan, L.P. Ye, An improved tie force method for progressive collapse resistance design of reinforced concrete frame structures. Eng. Struct. 33(10) (2011) 2931–2942.

[25] D.C. Feng, S.C. Xie, J. Xu, K. Qian, Robustness quantification of reinforced concrete structures subjected to progressive collapse via the probability density evolution method, Eng. Struct. 202 (2020) 109877.

[26] Ministry of Housing and Urban-Rural Development of the People's Republic of China (MOHURD). Code for design of concrete structures. GB50010-2010. Beijing, China; 2010.

[27] Ministry of Housing and Urban-Rural Development of the People's Republic of China (MOHURD). Code for seismic design of buildings, GB50011-2010. Beijing, China; 2010.

[28] Y. Wu, J.E. Crawford, J.M. Magallanes, Performance of LS-DYNA concrete constitutive models, 12th Int. LS-DYNA Users Conf, Livermore Software Technology Corporation, Livermore, CA, 2012.

[29] J. Hallquist, LS-DYNA Keyword User’s Manual, Version 971, Livermore Software Technology Corp., Livermore, CA, 2007.

[30] CEB. CEB-FIP model code 1990. Thomas Telford; 1991.

[31] B.A Izzuddin, A.G Vlassis, A.Y Elghazouli, D.A Nethercot, Progressive collapse of multi-storey buildings due to sudden column loss — Part I: Simplified assessment framework, Eng. Struct. 30(5) (2008) 1309–18.

Captions of tables

Table 1-Reinforcement properties

Table 2-Study on different mesh sizes

Table 3-Model parameters of CSCM for FE models (Unit: N, mm and ms)

Table 4-Comparison of key results between test and FE model

Captions of figures

Fig. 1–Dimensions of specimen US (units: mm) [5]

Fig. 2–Test setup and instrumentation location in the referenced experiment [5]

Fig. 3–Numerical model of US-CL-1F

Fig. 4–Comparison of different mesh sizes

Fig. 5–General shape of concrete model yield surface

Fig. 6–Comparison of different concrete input parameters

Fig. 7–Unconfined uniaxial stress-strain curve of concrete based on CSCM

Fig. 8–Comparison of load-displacement curves between test and FE model

Fig. 9–Comparison of failure modes between test and FE model: (a) US [5]; (b) US-CL-1F

Fig. 10–Comparison of the crack distributions between test and FE model: (a) US [5]; (b) US-CL-1F

Fig. 11–Details of numerical model for load distribution rig

Fig. 12–Layout of the loading system (unit: mm)

Fig. 13–Numerical model of US-UDL-1F

Fig. 14–Comparison of load-displacement curves between US-CL-1F and US-UDL-1F

Fig. 15–Failure modes of the slab in model US-UDL-1F: (a) Top surface of the slab; (b) Bottom surface of the slab

Fig. 16–Development of beam axial force: (a) US-CL-1F; (b) US-UDL-1F

Fig. 17–Contribution of each supporting column: (a) US-CL-1F; (b) US-UDL-1F

Fig. 18–Dynamic resistance of beam-slab substructures

Fig. 19–Numerical models: (a) US-CL-2F; (b) US-UDL-2F

Fig. 20–Comparison of load-displacement curves between CL and UDL conditions

Fig. 21–Development of shear force of corner column

Fig. 22–Comparison of load resistance from different stories with single-story substructure: (a) US-CL-2F; (b) US-UDL-2F

Fig. 23–Load resistance of each story under CL: (a) US-CL-3F; (b) US-CL-4F; (c) US-CL-5F

Fig. 24–Load resistance of each story under UDL: (a) US-UDL-3F; (b) US-UDL-4F

Fig. 25–Beam axial force of each story under CL: (a) US-CL-3F; (b) US-CL-4F; (c) US-CL-5F

Fig. 26–Beam axial force of each story under UDL: (a) US-UDL-3F; (b) US-UDL-4F

Table 1-Reinforcement properties

Items	Diameter (mm)	Yield strength (MPa)	Ultimate strength (MPa)	Elongation (%)	Yield strain (με)
R6	6	324	525	23	1543
T12	12	427	530	18	2135

Note: R6 represents plain bar with diameter of 6 mm; T12 represents deformed rebar with diameter of 12 mm.

Table 2-Study on different mesh sizes

Type	Mesh size 1	Mesh size 2	Mesh size 3
Mesh size of slabs (mm)	25×25×23.3	20×20×17.5	20×20×14
Mesh size of beams and columns (mm)	25×25×25	20×20×20	15×15×15
Mesh size of Reinforcements (mm)	25	20	15
Total number of solid elements	76672	152325	367990
Total number of beam elements	23330	29210	38708
Time consuming (s)	36241	43717	144940

Table 3-Model parameters of CSCM for FE models (Unit: N, mm and ms)

MID	**RO**	**NPLOT**	**INCRE**	**IRATE**	**ERODE**	**RECOV**	**ITRETRE**
1	0.00232	1	0.0	0	1.10	0.0	0
PRED							
0.0							
G	**K**	**ALPHA**	**THETA**	**LAMDA**	**BETA**	**HN**	**CH**
5000	5476	13.408	0.2751	10.5	0.01929	0.0	0.0
ALPHA1	**THETA1**	**LAMDA1**	**BETA1**	**ALPHA2**	**THETA2**	**LAMDA2**	**BETA2**
0.74735	0.001315	0.17	0.07639	0.66	0.001581	0.16	0.07639
R	**XD**	**W**	**D1**	**D2**			
5.0	87.8	0.05	2.5e-4	3.492e-7			
B	**GFC**	**D**	**GFT**	**GFS**	**PWRC**	**PWRT**	**PMOD**
100.0	3.308	0.1	0.06616	0.03308	5.0	1.0	0.0
ETA0C	**NC**	**ETAOT**	**NT**	**OVERC**	**OVERT**	**SRATE**	**REP0W**
0.0	0.0	0.0	0.0	0.0	0.0	0.0	0.0

Table 4-Comparison of key results between test and FE model

Results Source	Critical Displacement (mm)		Critical Load (kN)		
	YL	PL	YL	PL	UL
Test	50	85.2	35	43.5	14.1
FEM	46.8	83.6	37.1	43.7	13.6
FEM/Test	0.936	0.981	1.06	1.005	0.965

Note: YL, PL, and UL represent yield load, peak load, and ultimate load, respectively.

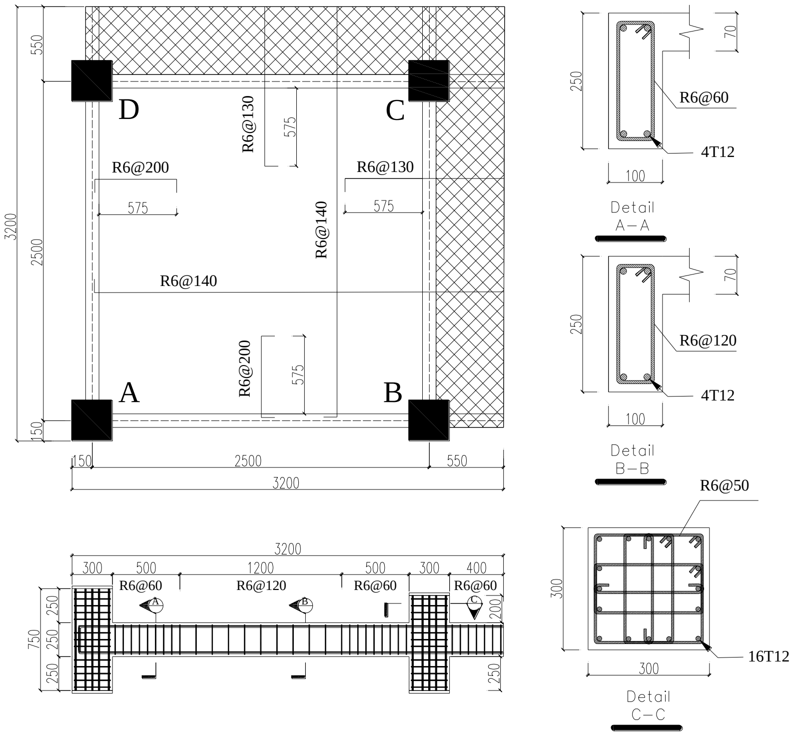

Fig. 1 Dimensions of Specimen US (units: mm) [5]

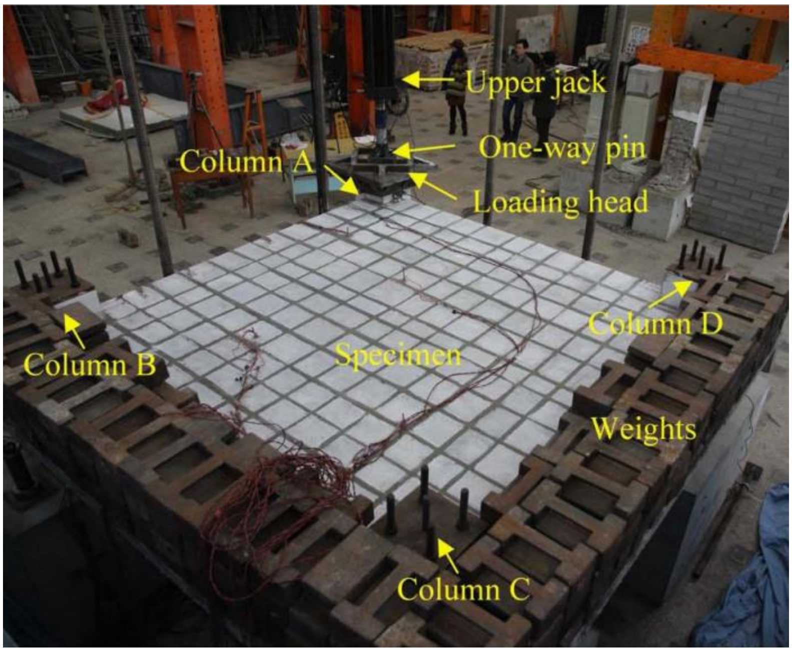

Fig. 2 Test setup and instrumentation location in the referenced experiment [5]

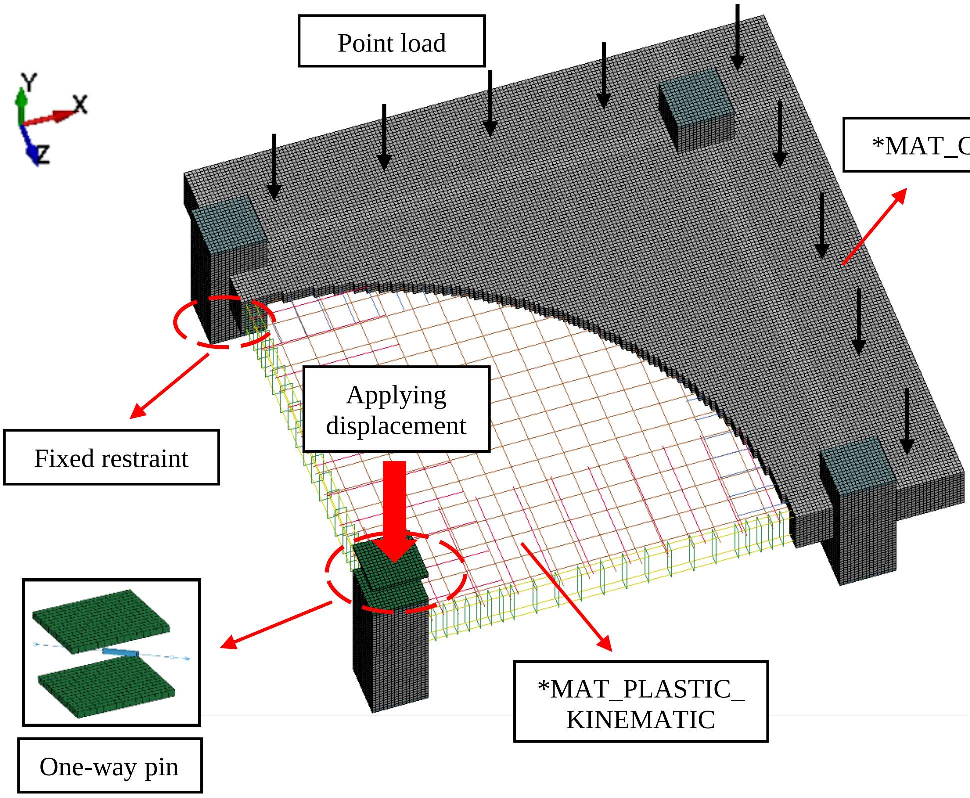

Fig. 3 Numerical model of US-CL-1F

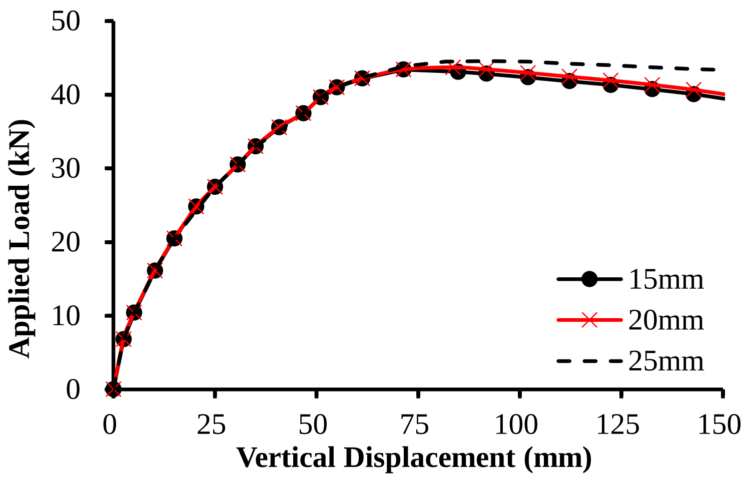

Fig. 4 Comparison of different mesh sizes

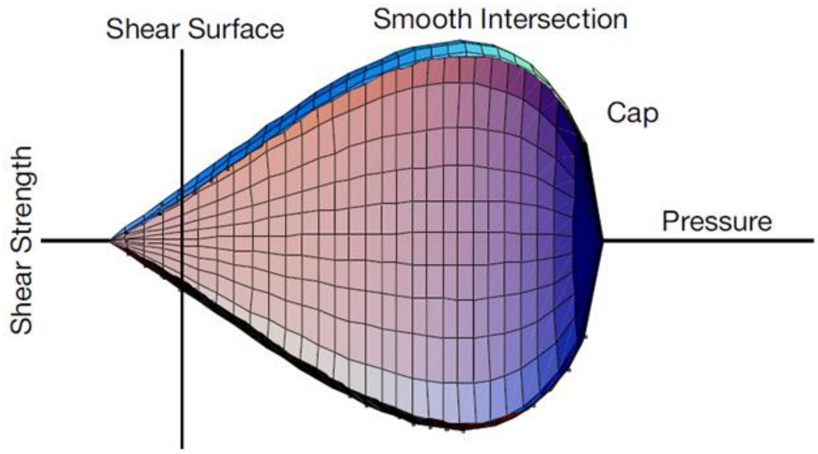

Fig. 5 General shape of concrete model yield surface

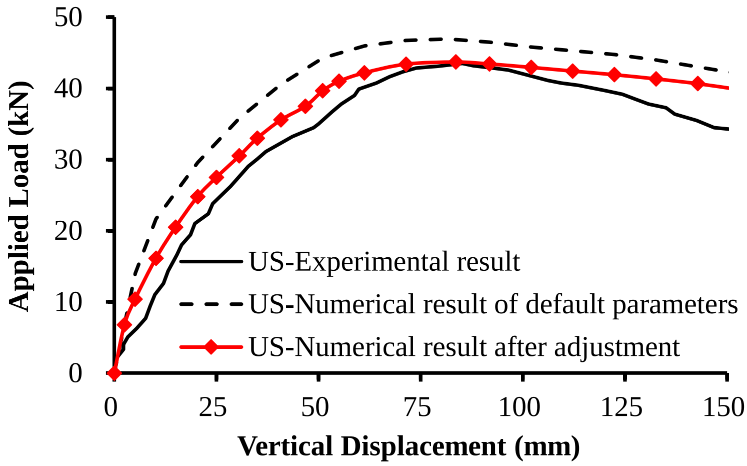

Fig. 6 Comparison of different concrete input parameters

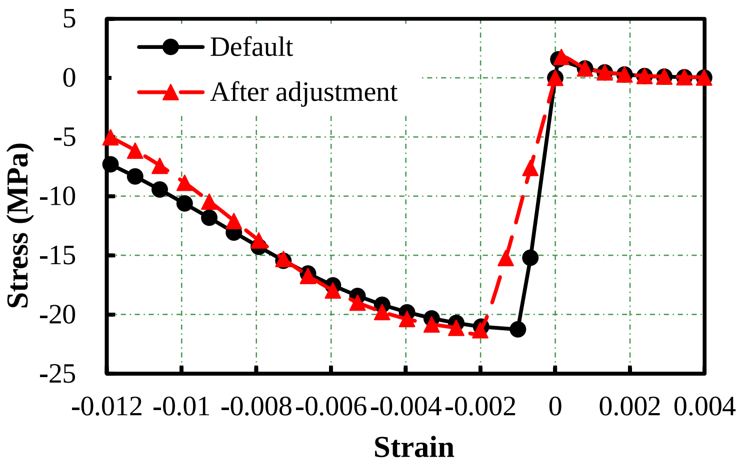

Fig. 7 Unconfined uniaxial stress-strain curve of concrete based on CSCM

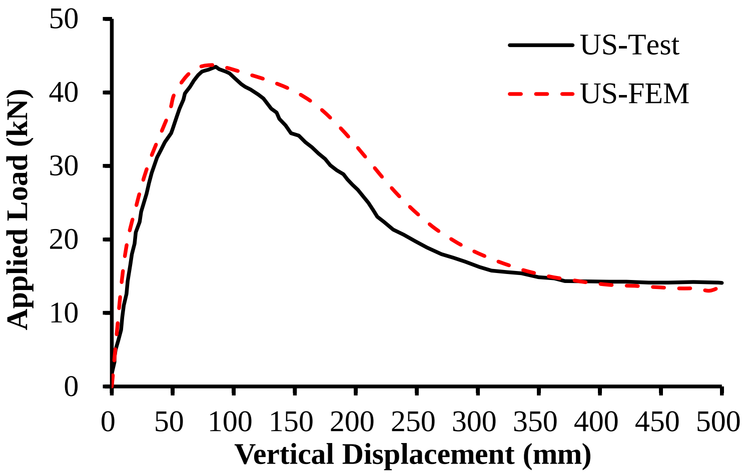

Fig. 8 Comparison of load-displacement curves between test and FE model

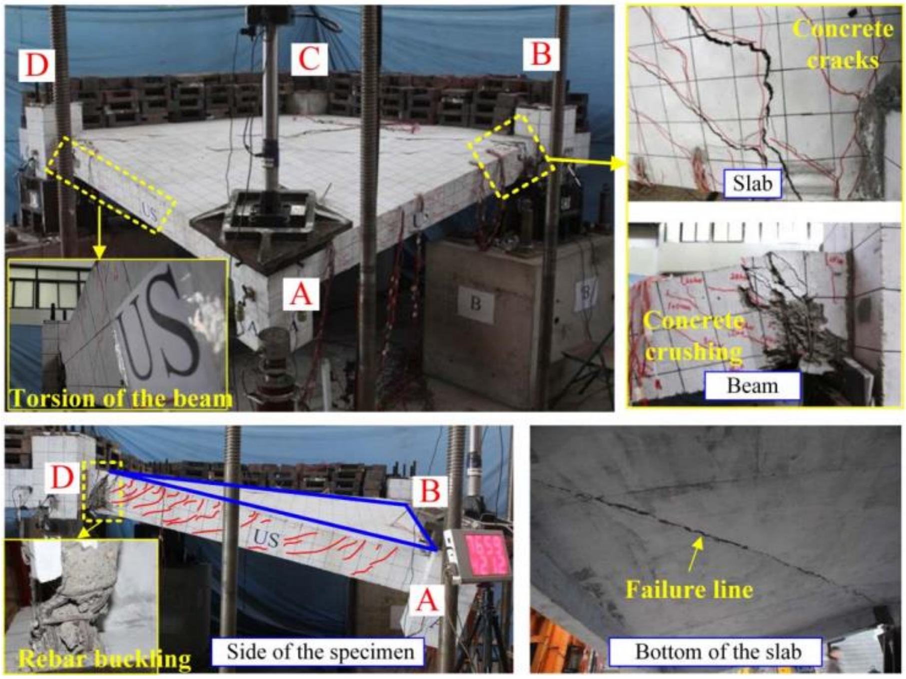

(a)

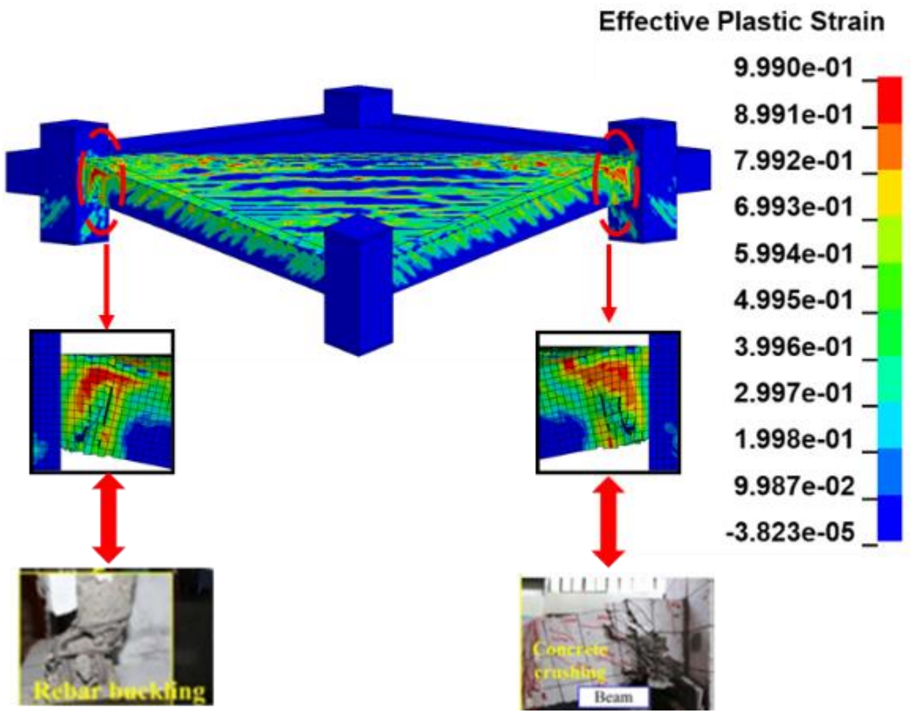

(b)

Fig. 9 Comparison of failure modes between test and FE model: (a) US [5]; (b) US-CL-1F

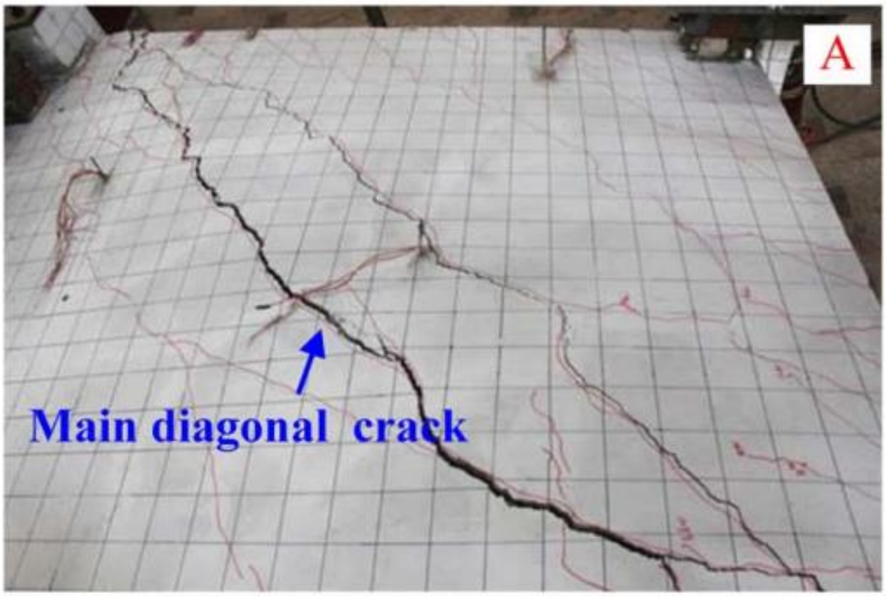

(a)

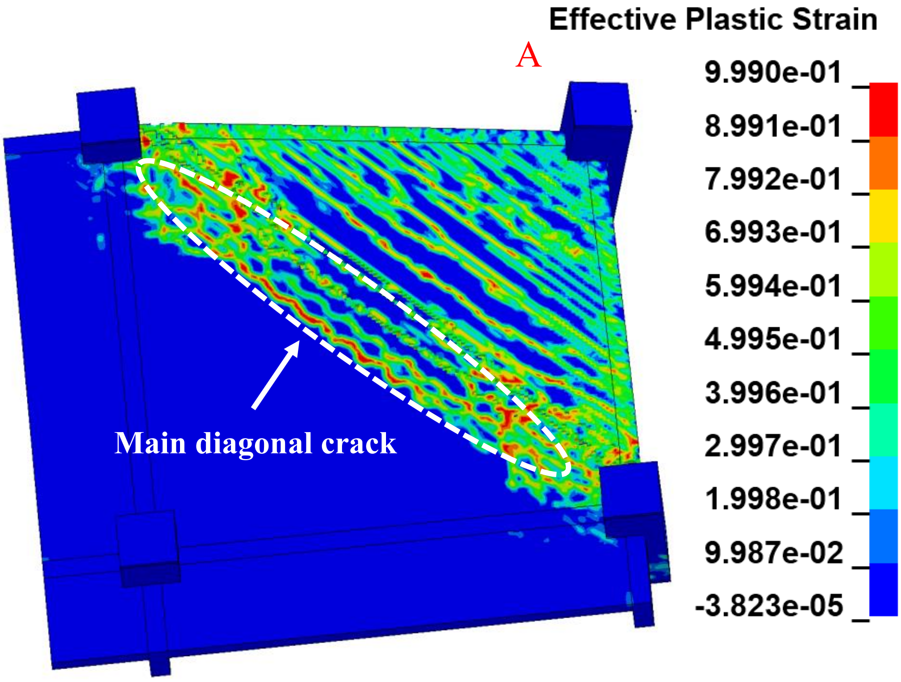

(b)

Fig. 10 Comparison of the crack distributions between test and FE model: (a) US [5]; (b) US-CL-1F

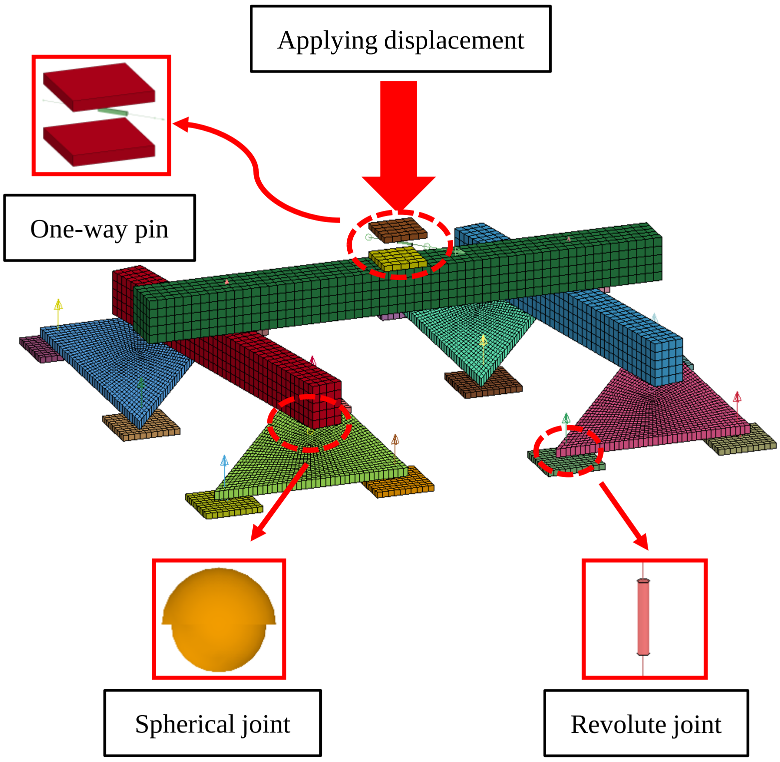

Fig. 11 Details of numerical model for load distribution rig

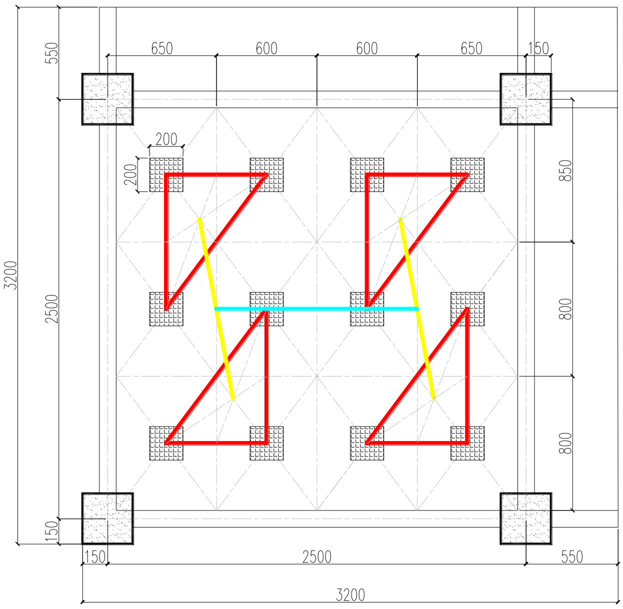

Fig. 12 Layout of the loading system (unit: mm)

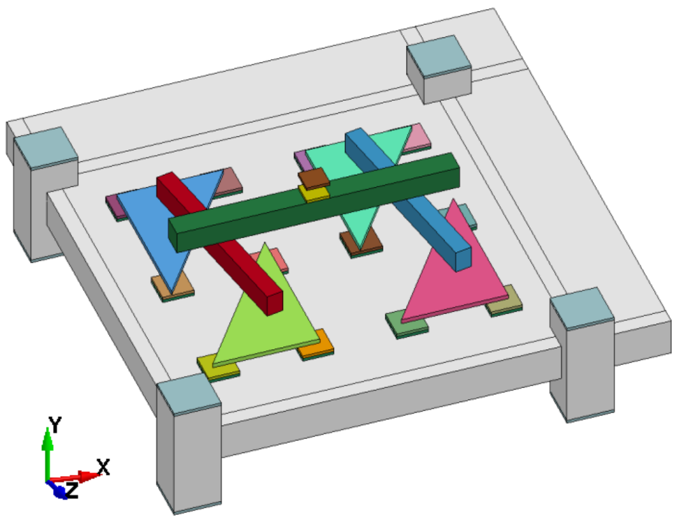

Fig. 13 Numerical model of US-UDL-1F

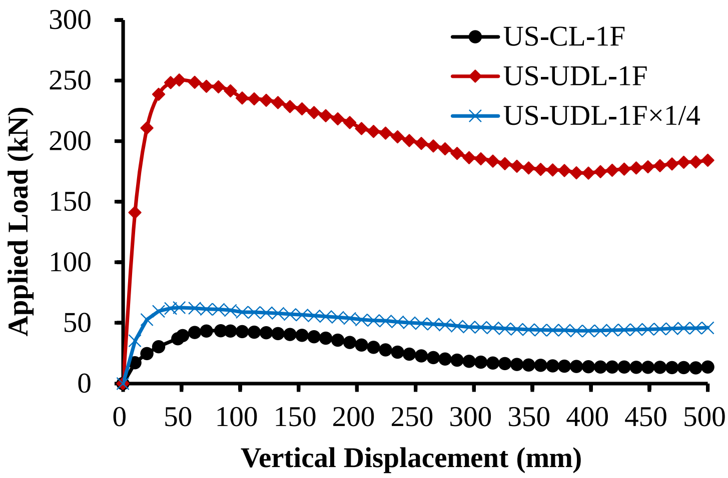

Fig. 14 Comparison of load-displacement curves between US-CL-1F and US-UDL-1F

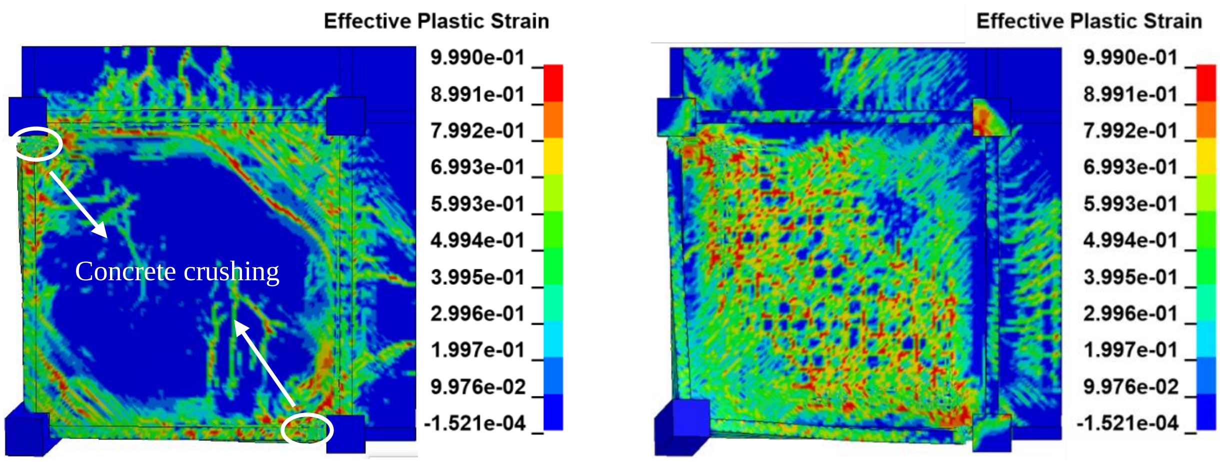

(a) (b)

Fig. 15 Failure modes of the slab in model US-UDL-1F: (a) Top surface of the slab; (b) Bottom surface of the slab

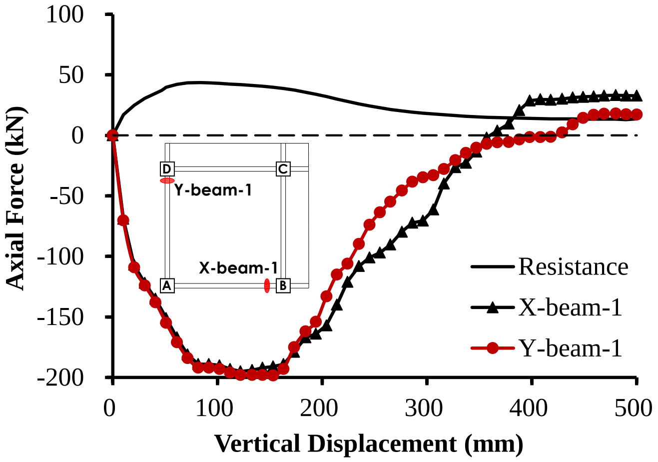

(a)

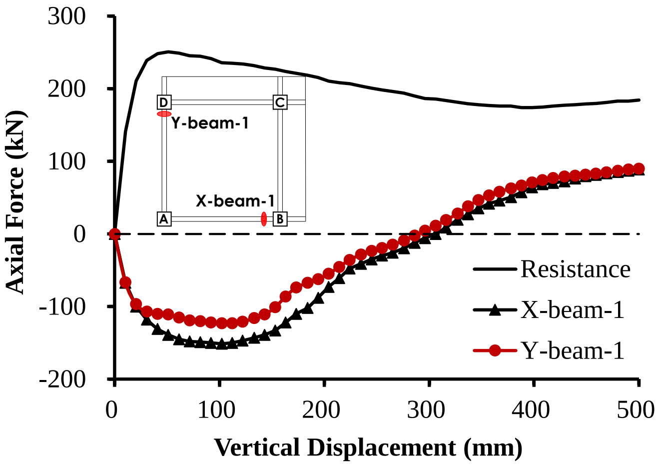

(b)

Fig. 16 Development of beam axial force: (a) US-CL-1F; (b) US-UDL-1F

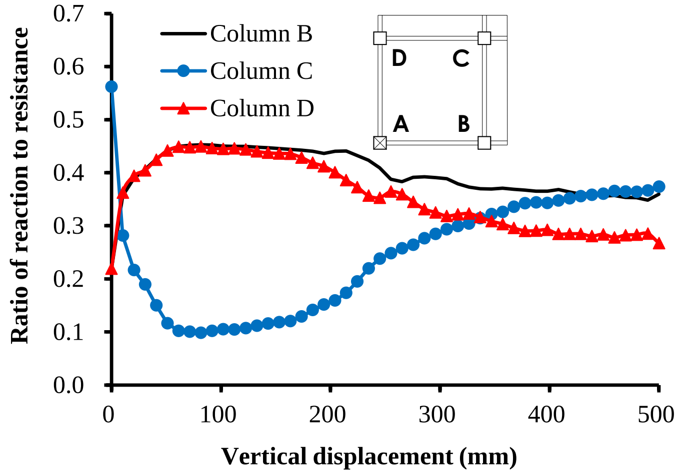

(a)

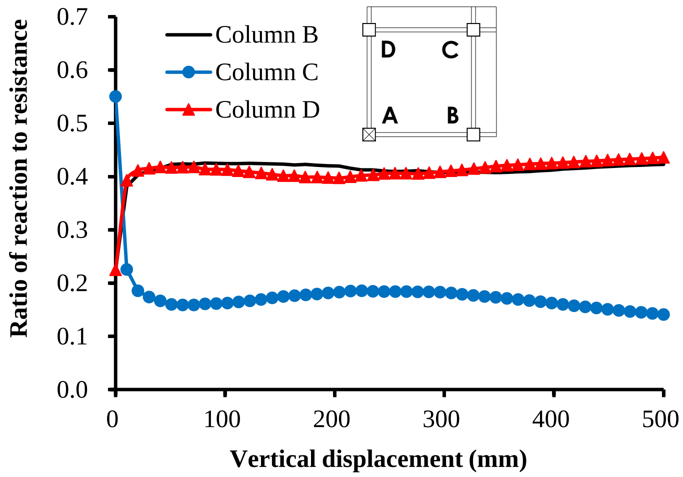

(b)

Fig. 17 Contribution of each supporting column: (a) US-CL-1F; (b) US-UDL-1F

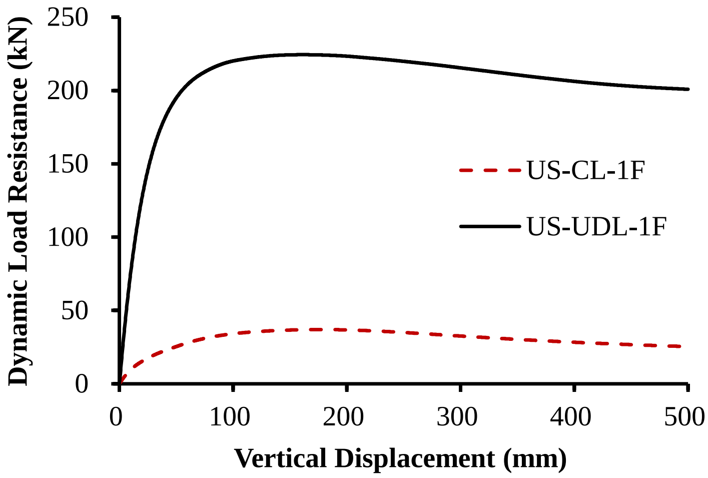

Fig. 18 Dynamic resistance of beam-slab substructures

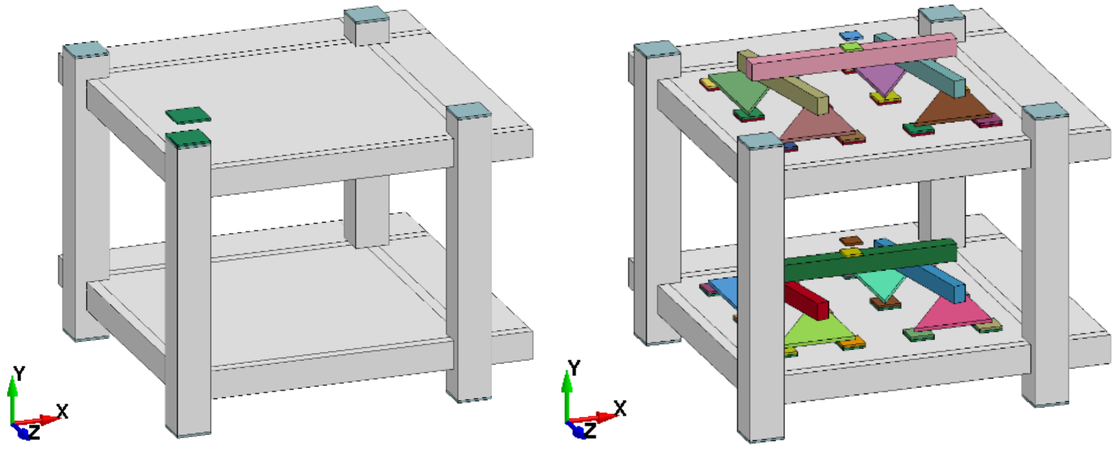

(a) (b)

Fig. 19 Numerical models: (a) US-CL-2F; (b) US-UDL-2F

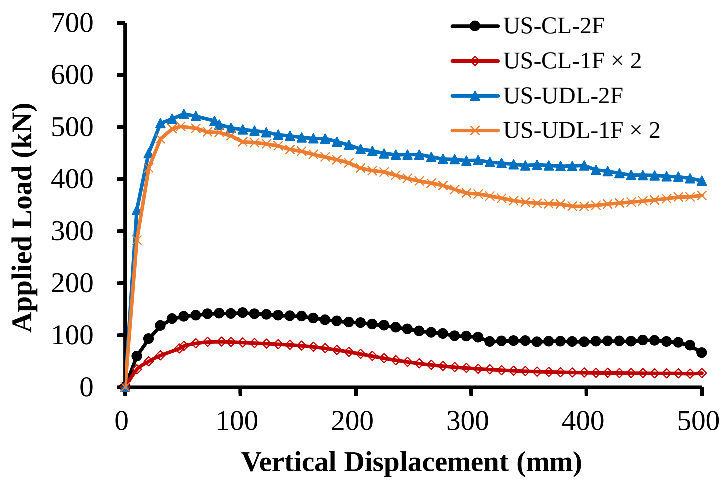

Fig. 20 Comparison of load-displacement curves between CL and UDL conditions

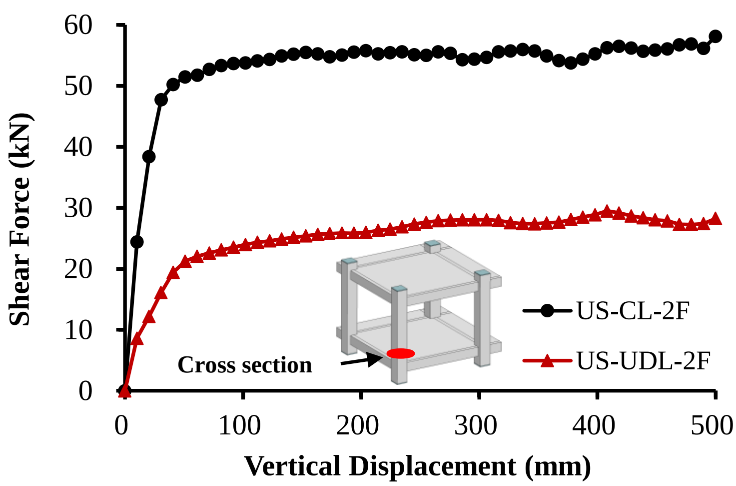

Fig. 21 Development of shear force of corner column

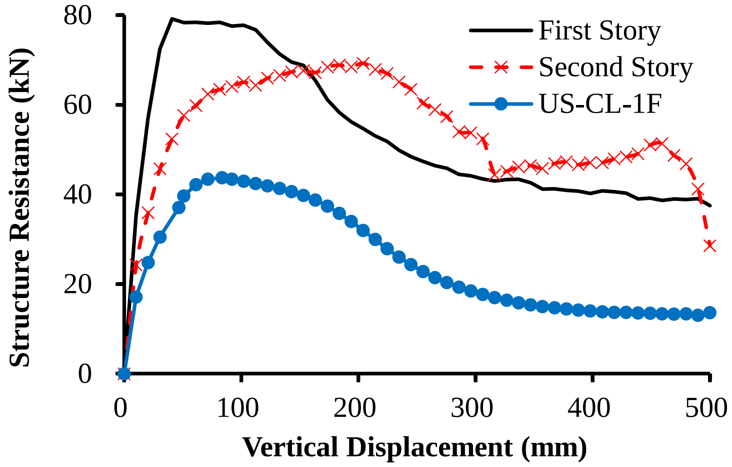

(a)

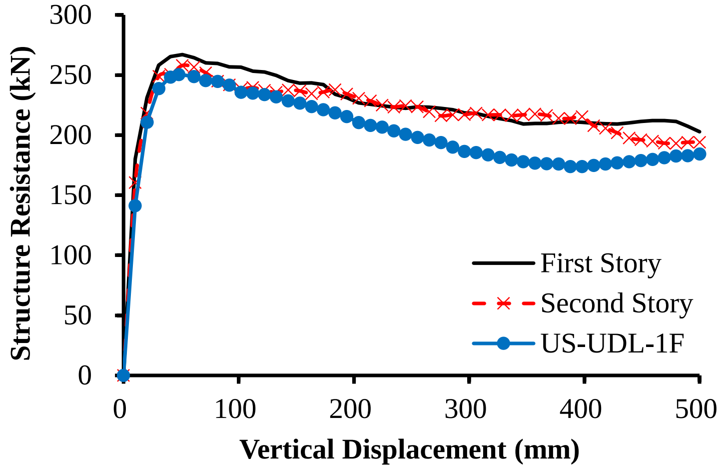

(b)

Fig. 22 Comparison of load resistance from different stories with single-story substructure:

(a) US-CL-2F; (b) US-UDL-2F

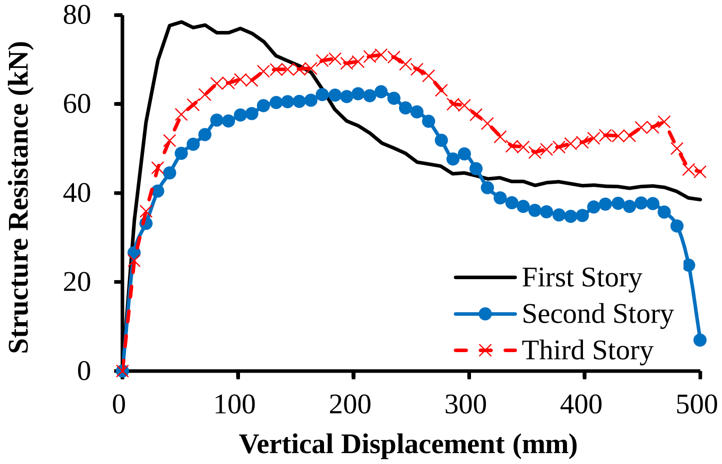

(a)

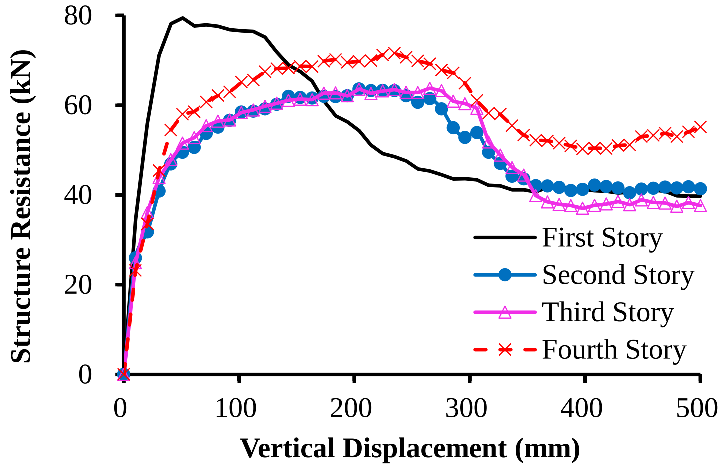

(b)

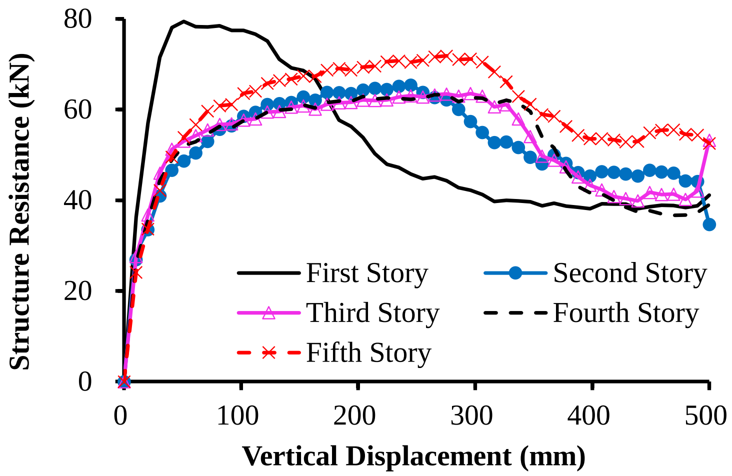

(c)

Fig. 23 Load resistance of each story under CL: (a) US-CL-3F; (b) US-CL-4F; (c) US-CL-5F

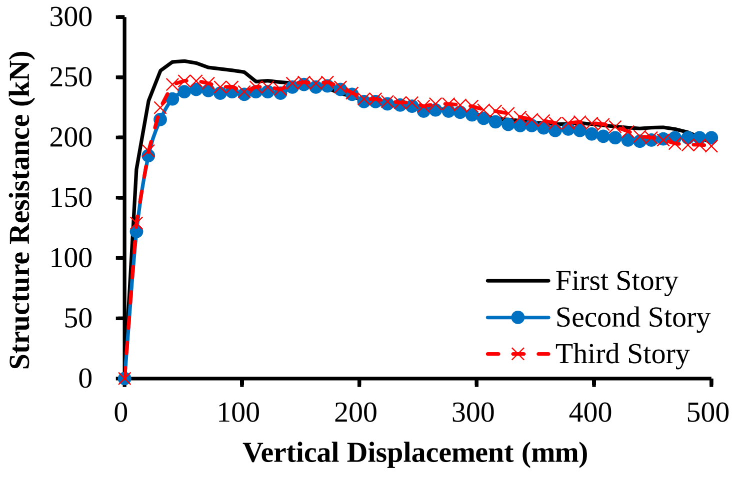

(a)

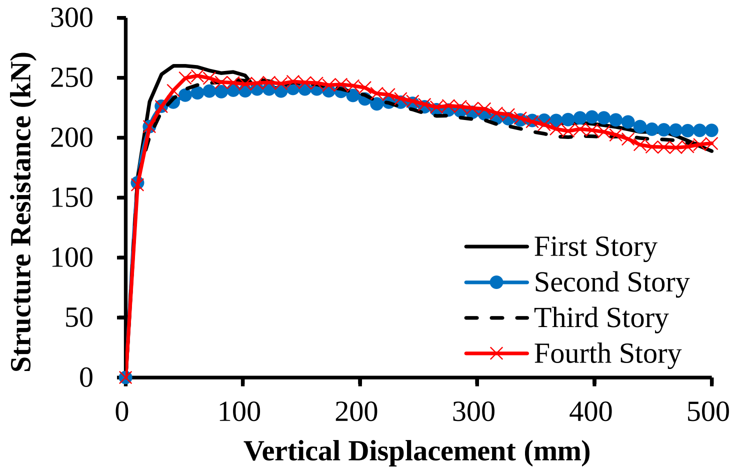

(b)

Fig. 24 Load resistance of each story under UDL: (a) US-UDL-3F; (b) US-UDL-4F

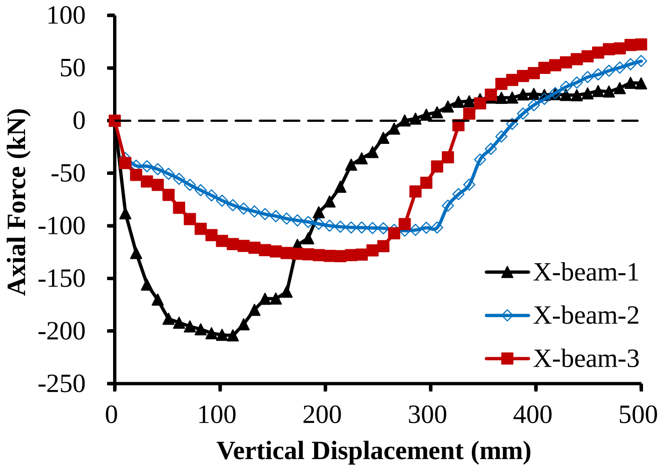

(a)

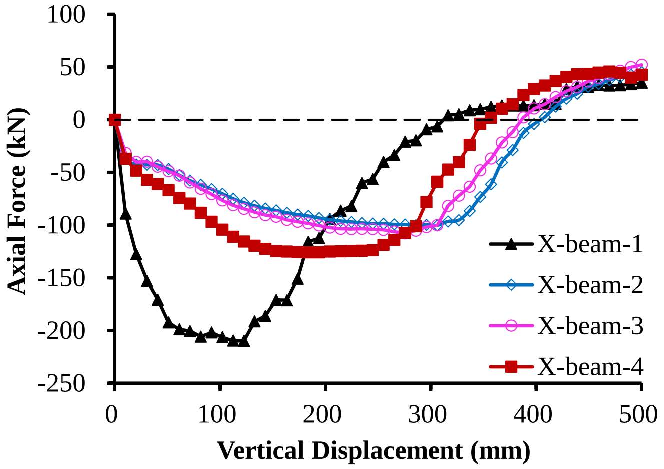

(b)

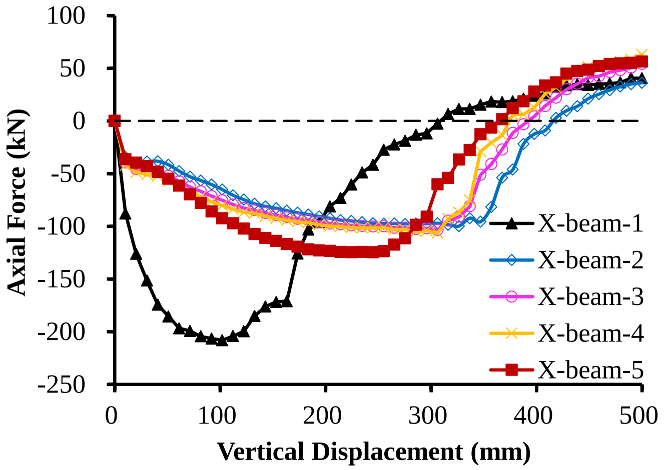

(c)

Fig. 25 Beam axial force of each story under CL: (a) US-CL-3F; (b) US-CL-4F; (c) US-CL-5F

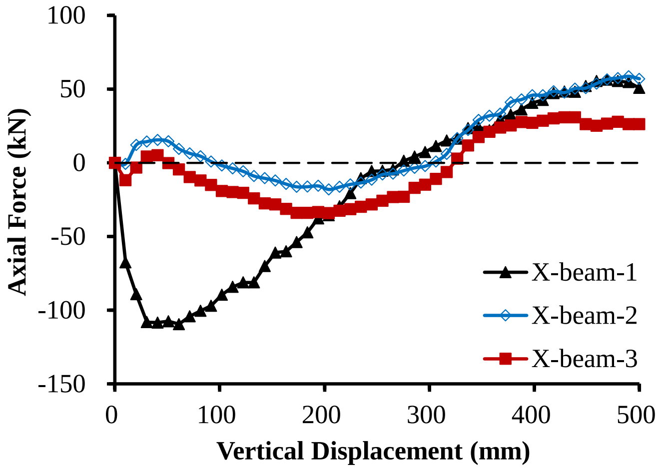

(a)

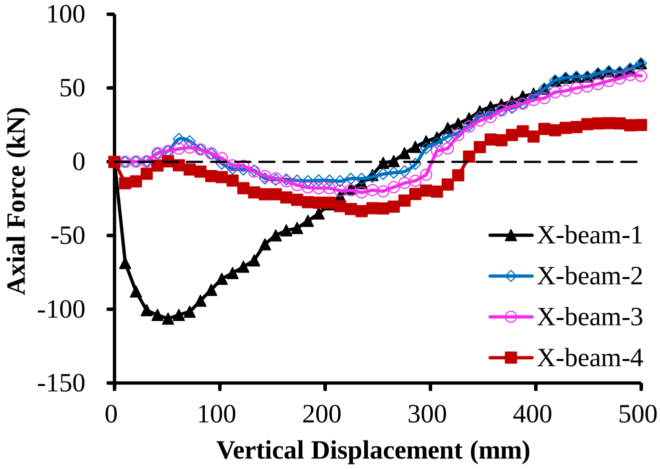

(b)

Fig. 26 Beam axial force of each story under UDL: (a) US-UDL-3F; (b) US-UDL-4F